

DETERMINATION OF STELLAR PARAMETERS FOR FGK-DWARF STARS: THE NIR  
APPROACH

by

Daniel Thaagaard Andreasen

A thesis submitted in conformity with the requirements  
for the degree of Doctor of Philosophy  
Graduate Department of Departamento de Física e Astronomia  
University of Porto

© Copyright 2017 by Daniel Thaagaard Andreasen

## **Dedication**

*To Linnea, Henriette, and Rico*

*For always supporting me*

## Acknowledgements

Lorem ipsum dolor sit amet, consectetur adipiscing elit. Ut purus elit, vestibulum ut, placerat ac, adipiscing vitae, felis. Curabitur dictum gravida mauris. Nam arcu libero, nonummy eget, consectetur id, vulputate a, magna. Donec vehicula augue eu neque. Pellentesque habitant morbi tristique senectus et netus et malesuada fames ac turpis egestas. Mauris ut leo. Cras viverra metus rhoncus sem. Nulla et lectus vestibulum urna fringilla ultrices. Phasellus eu tellus sit amet tortor gravida placerat. Integer sapien est, iaculis in, pretium quis, viverra ac, nunc. Praesent eget sem vel leo ultrices bibendum. Aenean faucibus. Morbi dolor nulla, malesuada eu, pulvinar at, mollis ac, nulla. Curabitur auctor semper nulla. Donec varius orci eget risus. Duis nibh mi, congue eu, accumsan eleifend, sagittis quis, diam. Duis eget orci sit amet orci dignissim rutrum.

Nam dui ligula, fringilla a, euismod sodales, sollicitudin vel, wisi. Morbi auctor lorem non justo. Nam lacus libero, pretium at, lobortis vitae, ultricies et, tellus. Donec aliquet, tortor sed accumsan bibendum, erat ligula aliquet magna, vitae ornare odio metus a mi. Morbi ac orci et nisl hendrerit mollis. Suspendisse ut massa. Cras nec ante. Pellentesque a nulla. Cum sociis natoque penatibus et magnis dis parturient montes, nascetur ridiculus mus. Aliquam tincidunt urna. Nulla ullamcorper vestibulum turpis. Pellentesque cursus luctus mauris.

## Abstract

Nam dui ligula, fringilla a, euismod sodales, sollicitudin vel, wisi. Morbi auctor lorem non justo. Nam lacus libero, pretium at, lobortis vitae, ultricies et, tellus. Donec aliquet, tortor sed accumsan bibendum, erat ligula aliquet magna, vitae ornare odio metus a mi. Morbi ac orci et nisl hendrerit mollis. Suspendisse ut massa. Cras nec ante. Pellentesque a nulla. Cum sociis natoque penatibus et magnis dis parturient montes, nascetur ridiculus mus. Aliquam tincidunt urna. Nulla ullamcorper vestibulum turpis. Pellentesque cursus luctus mauris.

## Resumo

Nam dui ligula, fringilla a, euismod sodales, sollicitudin vel, wisi. Morbi auctor lorem non justo. Nam lacus libero, pretium at, lobortis vitae, ultricies et, tellus. Donec aliquet, tortor sed accumsan bibendum, erat ligula aliquet magna, vitae ornare odio metus a mi. Morbi ac orci et nisl hendrerit mollis. Suspendisse ut massa. Cras nec ante. Pellentesque a nulla. Cum sociis natoque penatibus et magnis dis parturient montes, nascetur ridiculus mus. Aliquam tincidunt urna. Nulla ullamcorper vestibulum turpis. Pellentesque cursus luctus mauris.

# Contents

<b>List of Tables</b>	<b>vii</b>
<b>List of Figures</b>	<b>viii</b>
<b>1 Introduction</b>	<b>1</b>
1.1 Exoplanets . . . . .	2
1.2 Planet host stars . . . . .	2
1.3 This thesis . . . . .	2
<b>2 Theory</b>	<b>3</b>
2.1 Stellar structure . . . . .	3
2.2 Stellar atmosphere . . . . .	4
2.2.1 Atmosphere models . . . . .	6
2.2.2 Radiative transfer code - <b>MOOG</b> . . . . .	8
2.2.3 The equivalent width . . . . .	8
2.2.3.1 Temperature dependence . . . . .	8
2.2.3.2 Pressure dependence . . . . .	9
2.2.3.3 Abundance dependence . . . . .	11
2.2.3.4 Microturbulence . . . . .	13
2.3 Line list and atomic data . . . . .	14
2.4 Spectrographs . . . . .	15
<b>3 Deriving stellar parameters</b>	<b>16</b>
3.1 Photometry . . . . .	16
3.1.1 InfraRed Flux Method - IRFM . . . . .	16
3.1.2 $T_{\text{eff}}$ -colour-[Fe/H] calibration . . . . .	17
3.1.3 Asteroseismology . . . . .	18
3.2 Spectroscopy . . . . .	19
3.2.1 Synthesis . . . . .	19
3.3 <b>FASMA</b> . . . . .	20
3.3.1 Ingredients . . . . .	20
3.3.2 Wrapper for <b>ARES</b> . . . . .	21
3.3.3 Interpolation of atmosphere models . . . . .	22
3.3.4 Minimization . . . . .	23

3.3.5	Error estimate . . . . .	26
<b>4</b>	<b>Results for FGK stars</b>	<b>27</b>
4.1	The creation of a NIR line list . . . . .	27
4.1.1	First version . . . . .	27
4.1.1.1	Visual removal of lines . . . . .	28
4.1.1.2	Synthetic investigation . . . . .	28
4.1.1.3	Calibrating $\log gf$ . . . . .	29
4.1.2	Second version . . . . .	29
4.2	HD20010 . . . . .	29
4.2.1	First analysis . . . . .	29
4.2.2	Second analysis . . . . .	31
4.3	Arcturus . . . . .	32
4.4	10 Leo . . . . .	32
4.5	Synthetic cool stars . . . . .	34
4.6	Parameter dependence on EP cut . . . . .	34
<b>5</b>	<b>Future work</b>	<b>35</b>
	<b>Bibliography</b>	<b>36</b>

# List of Tables

4.1 Results for the three stars with first set of parameters are the literature values as presented in Table. ??, second set of parameters are results with  $\log g$  set to the same value during the minimization procedure as found in the literature (fixed), and last set of parameters are with all parameters free during the minimization procedure. . . . . 31



# List of Figures

2.1	Energy levels for hydrogen, $E_n = \frac{-13.6 \text{ eV}}{n^2}$ . . . . .	7
2.2	An absorption line centred at $\lambda_0$ normalised at the flux level $F_c$ . The area of the absorption line to the left is equal to the blue shaded area in the rectangle to the right with width EW. . . . .	9
2.3	The EW for a Fe I and Fe II line with increasing $T_{\text{eff}}$ . The two lines have similar EW in the Sun and are found in the optical part of the spectrum. The vertical line show the solar $T_{\text{eff}}$ . . . . .	10
2.4	<i>Upper panel:</i> Curve of growth for same Fe II used in Figure 2.3 for four different $\log g$ values. Here it is the weak lines mostly affected by the change in $\log g$ . <i>Lower left panel:</i> Synthetic spectra of the same line. The colour scale is the same. <i>Lower right:</i> The abundance for the line at different $\log g$ . A strong correlation (0.40) is seen. . . . .	12
2.5	<i>Upper panel:</i> Curve of growth of the same Fe I line as used in Figure 2.3. Four points are marked which is shown in the <i>lower panel</i> as a synthetic spectral line. The RW (proxy for EW) is clearly increasing with $\log gf$ (proxy for abundance). . . . .	13
2.6	Curve of growth for three different values of $\xi_{\text{micro}}$ . The EW is increasing with increasing $\xi_{\text{micro}}$ . . . . .	14
3.1	Measured and calculated flux from the Sun at infrared wavelengths. Data from Table 2 in <a href="#">Blackwell and Shallis (1977)</a> . Mean solar radius from this data is $1.011R_{\odot}$ , and mean solar $T_{\text{eff}} = 5963 \text{ K}$ using Equation 3.1. . . . .	17
3.2	Mass and radius from asteroseismic scaling relation. The colour is the mass and radius for the upper and lower panel, respectively. . . . .	19
3.3	Model atmosphere grid from <a href="#">Kurucz (1993)</a> at $[\text{Fe}/\text{H}] = 0.00$ between 3000 K and 10 000 K. The grid extends to higher $T_{\text{eff}}$ , but these are not considered in this thesis. . . . .	22
3.4	The abundances of Fe I for the planet host star: HATS-1. Upper plot: Converged parameters (see text for stellar parameters for this star). Middle plot: Converged parameters with 0.5 km/s added to $\xi_{\text{micro}}$ . Lower plot: Converged parameters with 500 K added to $T_{\text{eff}}$ . . . . .	24
3.5	Overview of the minimization for FASMA . Credit: <a href="#">Andreasen et al. (2017b)</a> . . . . .	26
4.1	Parameters for Arcturus, 10 Leo, and HD 20010 (revisited in this paper). The blue points show the literature values from the PASTEL database as discussed in the text. The green points are the derived values with $\log g$ fixed to the literature value, and the red points show the derived parameters when $\log g$ is also derived. . . . .	33

# Chapter 1

## Introduction

Effective temperature ( $T_{\text{eff}}$ ), surface gravity ( $\log g$ ), and metallicity ( $[M/H]$ , where iron is normally used as a proxy) are fundamental atmospheric parameters necessary to characterise a single star, and to determine other indirectly fundamental parameters such as mass, radius, and age from stellar evolution models (see e.g. [Baraffe et al., 2015](#); [Dotter et al., 2008](#); [Girardi et al., 2000](#)). Precise and accurate stellar parameters are also essential in exoplanet searches. Planetary radius and mass are mainly found from transit lightcurve analysis and radial velocity analysis, respectively. The determination of the mass of the planet implies a knowledge of the stellar mass, while the measurement of the radius of the planet is dependent on our capability to derive the radius of the star (see e.g. [Ammler-von Eiff et al., 2009](#); [Torres et al., 2012, 2008](#)).

The derivation of precise stellar atmospheric parameters is not a simple task. Different approaches often lead to discrepant results (see e.g. [Lebzelter et al., 2012](#); [Santos et al., 2013](#); [Torres et al., 2010](#)). Interferometry is usually considered an accurate method for deriving stellar radii (see e.g. [Boyajian et al., 2012](#)); however, it is only applicable for bright nearby stars. Asteroseismology, on the other hand, reveals the inner stellar structure by observing the stellar pulsations at the surface. From asteroseismology it is possible to measure the surface gravity and mean density, and therefore to calculate mass and radius with high precision (see e.g. [Kjeldsen and Bedding, 1995](#)). However, for stars on the main sequence asteroseismic methods can typically only be applied to FG stars, since the oscillation modes of K and M dwarfs are likely too weak to be detected even with high precision spectroscopy or photometry. Moreover, the effective temperature is needed when applying asteroseismology in order to obtain the surface gravity and the mean density.

A crucial parameter for the indirect determination of stellar bulk properties is the  $T_{\text{eff}}$ . In that respect, the infrared flux method (IRFM) has proven to be reliable for FGK dwarf and subgiant stars. For higher accuracy the IRFM needs a priori knowledge of the bolometric flux, reddening, surface gravity, and stellar metallicity ([Blackwell and Shallis, 1977](#); [Casagrande et al., 2010](#); [Ramírez and Meléndez, 2005a](#)).

Finally, the use of high resolution spectroscopy along with stellar atmospheric models is an extensively tested method that allows the derivation of the fundamental parameters of a star (see e.g. [Santos et al., 2013](#); [Valenti and Fischer, 2005](#)). The procedure depends on the quality of the spectra, their resolution, and wavelength region. A fit to the overall spectrum can be applied for all spectral resolutions, but are often time consuming (see e.g. [Recio-Blanco et al., 2006](#); [Tsantaki et al., 2014](#)). For resolutions higher than  $\lambda/\Delta\lambda \sim 20\,000$  we can apply the equivalent width (EW) method (see e.g. [Andreasen et al., 2017b](#);

[Tsantaki et al., 2013](#), for details). However, while the latter approach is often faster than the synthetic fitting, it requires higher quality spectra, and the star to be slow rotating (below 10 km/s to 15 km/s).

Standard procedures are often used to derive stellar atmospheric parameters from high quality spectra in the optical (see e.g. [Sousa et al., 2008](#); [Valenti and Fischer, 2005](#)). With the advancement of high resolution near-infrared (NIR) instruments, we will now be able to use a similar technique to that used in the optical part of the spectrum (see e.g. [Bensby et al., 2014](#); [Meléndez and Barbuy, 1999](#); [Mucciarelli et al., 2013](#); [Sousa et al., 2008](#); [Tsantaki et al., 2013](#)). At the moment, the GIANO spectrograph installed at *Telescopio Nazionale Galileo* (TNG) is already available ([Origlia et al., 2014](#)), as is the *infrared Doppler instrument* (IRD) installed at the Subaru telescope ([Kotani et al., 2014](#)), *Calar Alto high-Resolution search for M dwarfs with Exoearths with Near-infrared and optical Échelle Spectrographs* (CARMENES) for the 3.5 m telescope at Calar Alto Observatory ([Quirrenbach et al., 2014](#)), and iShell at the *InfraRed Telescope Facility* ([Rayner et al., 2012, 2016](#)). Three new spectrographs are planned for the near future: 1) The *CRYogenic InfraRed Echelle Spectrograph Upgrade Project* (CRIRES+) at the *Very Large Telescope* (VLT) ([Follert et al., 2014](#)) with expected first light in 2017, 2) *un SpectroPolarimètre Infra-Rouge A Near-InfraRed Spectropolarimeter* (SPIrou) at *The Canada-France-Hawaii Telescope* (CFHT) ([Artigau et al., 2014](#); [Delfosse et al., 2013](#)) with expected first light in 2017 as well, and 3) *Near Infrared Planet Searcher* NIRPS at the ESO 3.6 m telescope in La Silla ([Conod et al., 2016](#)). The spectral resolutions for these spectrographs range between 50 000 and 100 000.

With the advance of the next generation NIR spectrographs, we are still preparing the data analysis of stellar spectra, in particular how to get reliable atmospheric parameters (see e.g. [Andreasen et al., 2016](#); [Lindgren et al., 2016](#); [Önehag et al., 2012](#)). The analysis of stellar spectra is well understood for FGK stars in the optical part of the spectrum, however some work still needs to be done for the NIR part.

We continue our series of studies to explore the use of the NIR domain to derive stellar parameters for FGK and M stars. In particular, here we analyse the atlas of Arcturus and the spectrum of 10 Leo. For the analysis we use the iron line list presented in [Andreasen et al. \(2016\)](#) (referred to as Paper I). In Paper I we successfully tested our method on a slightly hotter star than the Sun, while in this work we aim to test the method on cooler stars. The strength of the NIR domain over the optical becomes clear when we move towards the cooler stars. Here we see less continuum depression and line blending due to in particular molecular features. Moreover, the cooler stars emit more light in the NIR domain than the optical, and with the lightest stars being intrinsically faint, we thus obtain the majority of the flux here.

## 1.1 Exoplanets

## 1.2 Planet host stars

With the present diversity of exoplanets it becomes increasingly important to get an accurate and precise characterisation of the planets in order to study them in samples and on an individual level. An accurate and precise characterisation can give us an idea whether the planet is rocky, composed of water or gaseous.

## 1.3 This thesis

# Chapter 2

## Theory

“Begin at the beginning," the King said, very gravely, "and go on till you come to the end: then stop.”

Lewis Carroll, Alice in Wonderland

To encompass all theory regarding stellar structure, evolution, and their atmosphere is far beyond the scope of this thesis. Rather the theory needed is presented below with highlights on the most important aspects.

### 2.1 Stellar structure

The structure of a non-rotating spherical stars can be described by five rather simple differential equations (see e.g. [Kippenhahn and Weigert, 1994](#)) presented below:

#### 1. Equation of Continuity

Relation between the mass,  $m$ , the density,  $\rho$ , at a symmetric shell at radius  $r$

$$\boxed{\frac{\partial r}{\partial m} = \frac{1}{4\pi r^2 \rho}}. \quad (2.1)$$

#### 2. Equation of Hydrostatic Equilibrium

The equation of hydrostatic equilibrium shows how a star in equilibrium is balanced between two forces. The inward force from gravity and the outward force from pressure,  $P$ ,

$$\boxed{\frac{\partial P}{\partial m} = -\frac{Gm}{4\pi r^4}}. \quad (2.2)$$

When working with asteroseismology a time dependent perturbation to this equation is added (see e.g. [Aerts et al., 2010](#), for a thorough discussion). However, this term is neglected here.

### 3. Equation of Energy Conservation

The equation of energy conservation shows how the energy is produced and lost throughout the star.

$$\boxed{\frac{\partial l}{\partial m} = \varepsilon - \varepsilon_\nu + \varepsilon_g,} \quad (2.3)$$

where  $\varepsilon$  is the energy production in the centre of the star,  $\varepsilon_\nu$  is the energy lost by neutrinos which is always positive,  $\varepsilon_g$  is a source function of time-dependent terms, and  $l$  is the luminosity at  $m$ .  $\varepsilon_g$  comes from the fact that non-stationary shells can change its internal energy, and thus exchange mechanical energy with neighbouring shells.

### 4. Equation of Energy Transport

Energy transportation throughout the star is described with the following equation

$$\boxed{\frac{\partial T}{\partial m} = -\frac{GmT}{4\pi r^4 P} \nabla_{\text{rad}},} \quad (2.4)$$

where  $\nabla_{\text{rad}}$  is the radiative temperature gradient, and  $T$  is the temperature. The value of the temperature gradient compared to the radiative temperature gradient tells if the energy is transported by convection or radiation. In our Sun the outer layer are convective while the inner layer are radiative.

### 5. Equation of Chemical Composition

In this last equation we see the evolution of an element,  $X_i$ , when it reacts with other elements with reaction rates  $r_{ji}$  and  $r_{ik}$

$$\boxed{\frac{\partial X_i}{\partial t} = \frac{m_i}{\rho} \left( \sum_j r_{ji} - \sum_k r_{ik} \right).} \quad (2.5)$$

Note that this is the only time-dependent equation of the five presented.

These five fundamental equations are implemented in stellar evolutionary codes, which we will use in later chapters. The many different codes that exist take other things into account, e.g the star can rotate, and it may not always be in hydrostatic equilibrium (this is important if we want our star to pulsate). For simplicity we have only presented time-dependence in the Equation of Chemical Composition since timescales of rotation, pulsations, and activity are much shorter than the long timescale found in chemical composition changes.

## 2.2 Stellar atmosphere

Much of this Section is inspired by [Gray \(2005\)](#). While all the figures here were made by the author of this thesis, most of them can be found in [Gray \(2005\)](#) as well.

Stellar atmospheres are rather complex. This is where the energy produced in the interior of the stars are released. However, the atmosphere of a star is not transparent to all light, and some of the light is absorbed or scattered in the atmosphere. In the case of absorption the light will later be emitted in a random direction. This is seen as an absorption line in the stellar spectrum. The different elements in the atmosphere is the reason for absorbing light at specific wavelength. The strength of the absorption depends on the physical conditions in the atmosphere, the effective temperature ( $T_{\text{eff}}$ ), the pressure/gravity ( $\log g$ ), the overall metallicity ( $[\text{Fe}/\text{H}]$ ), the specific abundance of a given element if different from the overall metallicity ( $A$ ), and the atomic characteristics of the transition coursing the absorption line.

It is important to know the fraction of atoms excited to the  $n$ th energy level,  $N_n$ . This fraction is proportional to the statistical weight  $g_n$  and the Boltzmann factor and is described as:

$$\boxed{\frac{N_n}{N} = \frac{g_n}{u(T)} 10^{-\theta \chi_n}} \quad \text{Boltzmann}$$

This equation is also called the Boltzmann equation. Here  $N$  is the total number of atoms per unit volume,  $u(T) = \sum g_i e^{-\chi_i/kT}$  is the partition function,  $k$  is Boltzmann's constant,  $T$  is the temperature, and  $\chi_n$  is the excitation potential for the lower energy level.

While atoms can get excited following Boltzmann's equation above, they can also get ionized. The ionization ratio for a collision dominated gas (which is a good approximation for FGKM stars) is described by the Saha equation. This equation relate the ratio of atoms in state  $r$  to atoms in the excited state above for the same element,  $r + 1$ , in the following way:

$$\boxed{\frac{N_{r+1}}{N_r} = \frac{1}{P_e} \frac{(2\pi m_e)^{3/2} (kT)^{5/2}}{h^3} \frac{2u_{r+1}(T)}{u_r(T)} e^{-I/kT} = \frac{\Phi(T)}{P_e}} \quad \text{Saha}$$

here  $m_e$  is the electron mass,  $h$  is Planck's constant,  $I$  is the ionization potential of the neutral atom, and  $\Phi(T)$  is all not related to the electron pressure,  $P_e$ .

The atomic lines are characterised by a few quantum mechanical descriptors.

- The wavelength,  $\lambda$  of an absorption (or emission) describes the energy difference between the two energy levels where the transition occurs.
- The ionization state, e.g. Fe I describes iron in its atomic form, while Fe II describes iron in its first ionized form.
- The excitation potential  $\chi$ . This gives an idea how deep in the atmosphere a line is formed. If  $\chi$  is high, then higher temperatures (i.e. higher random motion and more collisions between the atoms) is required for forming the absorption line. These higher temperatures are found deeper in the atmosphere.
- The oscillator strength,  $\log gf$ , is related to the atomic transition probability.
- The damping coefficients, is a natural damping (also known as radiation damping) caused by the uncertainty of lifetime in an energy level according to Heisenberg's uncertainty principle. This is related to a uncertainty in the energy level and thus a natural broadening is introduced.

These are essential to know from either theoretical calculations or experiments. The oscillator strength is a quantity that is difficult to measure, and this is often changed when absorption lines are matched with real observations of e.g. the Sun. This is a way of calibrating a line list and will be described in detail in Section 2.3.

It is important to mention that one of the main differences between absorption lines at different wavelengths is the excitation potential. The energy levels of an atom gets denser packed as the energy level increase as shown in Figure 2.1 for hydrogen. For hydrogen the energy levels  $E_n$  follow the very simple formula from Bohr's atomic model,  $E_n = \frac{-13.6\text{eV}}{n^2}$ , where  $n$  is the principal quantum number, and 13.6 eV is the ionization energy for hydrogen, i.e. the minimum amount of energy required to ionize hydrogen. The energy levels for heavier atoms show a similar structure. The outer electron for a multi-electron atom is partially shielded from the nucleus by the inner electrons, and thus does not experience the full charge  $Z$  but rather an effective charge  $Z_{\text{eff}}$ , giving the expression

$$E_n = -hcR_{\infty} \frac{Z_{\text{eff}}^2}{n^2}, \quad (2.6)$$

where  $h$  is Planck's constant,  $c$  is the speed of light, and  $R_{\infty}$  is Rydberg's constant.

With increasing  $n$  the energy levels get closer, or in other words the photon required to excite an electron from one energy level to a neighbouring state will get redder. These redder photons used for exciting an atom are the absorption lines seen in the NIR. However, the excitation to the lower state is from thermal motion and not coursed by photons. Since tight energy levels require a highly excited lower state, the temperature required here are similar high, which means that the NIR lines are typically formed in the deeper layers of the atmosphere compared to absorption lines seen in the optical part of the spectrum.

The above discussed energy transitions are purely electronic, however there exists so called fine structure transitions as well. This is due to the spin of the electron (or magnetic moment) interacting with the orbital angular momentum of the electron. This leads to a splitting of the absorption line. In atoms there also exists an even finer structure, commonly known as the hyperfine structure. This structure arise due to the interaction between the magnetic field created by the electrons and the nuclear spin. These splittings are important to consider for some transitions and some atoms. For Fe the hyperfine structure is not important since the net nuclear spin of protons is 0 because there is an even number of protons, hence hyperfine structure is only important for atoms with an odd number of protons. There are other splitting and shift for spectral absorption lines like the Zeeman splitting coursed by an external magnetic field, and the Stark effect splitting a line due to an external electric field. These two last effect are minor and will not be discussed more, however it is worth noting that the Zeeman splitting can be used to measure the strength of a magnetic field in a star if this is strong enough.

### 2.2.1 Atmosphere models

In order to derive abundances or calculate a synthetic spectrum, two main things are needed: 1) And atmosphere model, and 2) a radiative transfer code that solves the equations above. There are different atmosphere models available. Throughout this thesis the ATLAS9 model atmosphere are used (Kurucz, 1993). Other mention-able atmosphere models includes MARCS models (Gustafsson et al., 2008) and the PHOENIX models (Husser et al., 2013). An atmosphere model is a description of the structure of the atmosphere. This description has a number of quantities. The atmosphere model grids that are

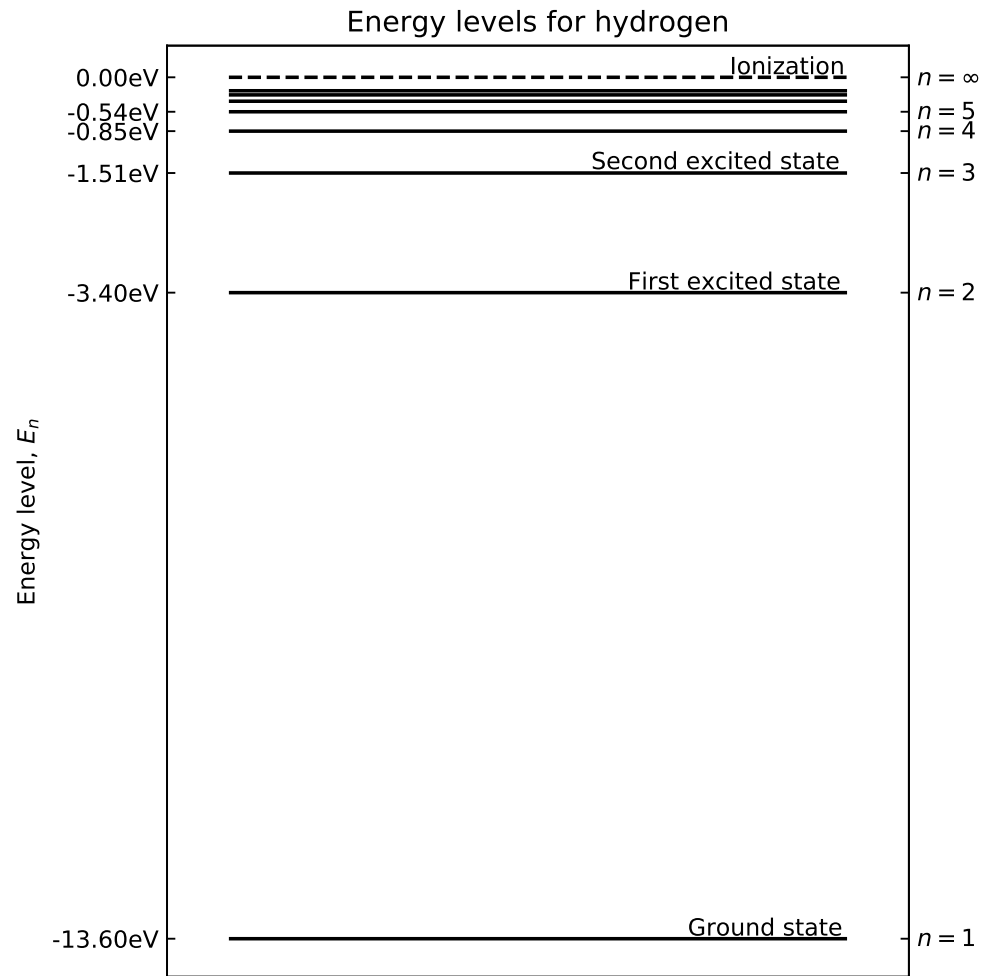


Figure 2.1: Energy levels for hydrogen,  $E_n = \frac{-13.6 \text{ eV}}{n^2}$ .



available and used here have 72 layers. Each layer includes physical quantities such as temperature, gas and electron pressure, the optical depth, etc. The models can be calculated on the fly, but it is common practise because of computational reasons to pre-calculate a grid of atmosphere models at certain  $T_{\text{eff}}$ ,  $\log g$ , and  $[\text{Fe}/\text{H}]$ . A specific atmosphere model is then obtained from this grid by interpolating from nearest neighbours. The interpolation code used throughout this work includes the four nearest neighbours in the  $T_{\text{eff}}$ -space, and the two nearest neighbours in both the  $\log g$ - and  $[\text{Fe}/\text{H}]$ -space, in total  $4 \times 2 \times 2 = 16$  atmosphere models to generate a single interpolated atmosphere model.

### 2.2.2 Radiative transfer code - MOOG

As mentioned above, a radiative transfer code is needed to solve the equations above. There are many different codes that does this. Here the MOOG code is used (Snedden, 1973). This code has different drivers, only some are used here.

- Derive a theoretical equivalent width (see Section 2.2.3 for details) for a given star, i.e. atmosphere model with a given set of atmospheric parameters.
- Derive line abundance from a measured equivalent width for a given model atmosphere.
- Calculate a synthetic spectrum for a given model atmosphere and atomic line list.
- Calculate the curve-of-growth for an atomic line.

There exists other drivers as well, but these are the ones used here. Some only for visualising the figures below.

### 2.2.3 The equivalent width

Measuring the equivalent width (EW) of spectral lines are important for some analysis of stellar spectra. The EW is a measure of the strength of the line, and dependent on the atmospheric conditions in where the spectral line is formed, such as  $T_{\text{eff}}$ ,  $\log g$ ,  $[\text{Fe}/\text{H}]$ , and  $\xi_{\text{micro}}$ .

The EW is mathematically described as integrating over the entire line, and assign this area to a rectangle from 0 to the continuum flux ( $F_c$ ) with the width, EW. This is illustrated in Figure 2.2 and the equation below:

$$EW = \int_0^\infty \frac{F_c - F(\lambda)}{F_c} d\lambda, \quad (2.7)$$

where  $\lambda$  is the wavelength. This integral is assuming there is only one single line, hence the integral is over all wavelength. In practice the integral is calculated in small windows around a spectral line. See Section 3.3.2 for more details on how this is performed in practice. The unit of the EW is the same as the wavelength used. Throughout this thesis we will use Ångström ( $1\text{\AA} = 0.1\text{ nm}$ ) for the wavelength, and mÅ for the EW.

#### 2.2.3.1 Temperature dependence

As mentioned above the EW depends on the atmospheric parameters. The dependence on  $T_{\text{eff}}$  is the strongest dependence. At low  $T_{\text{eff}}$  neutral elements, say Fe I, are the strongest lines as the number of

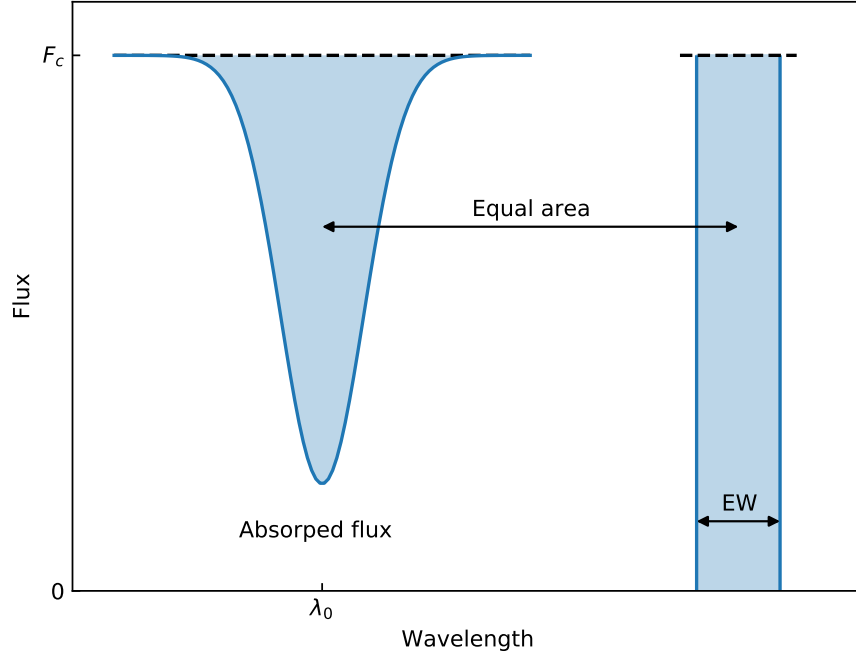


Figure 2.2: An absorption line centred at  $\lambda_0$  normalised at the flux level  $F_c$ . The area of the absorption line to the left is equal to the blue shaded area in the rectangle to the right with width EW.

ionized atoms are too small to contribute significantly to the EW. This is the result the Saha equation. As  $T_{\text{eff}}$  increases Fe I is converted into ionized Fe II. Slowly, as the number of Fe I decreases so does the EW, and likewise as the number of Fe II increases so does the EW. This goes on until second ionized atoms, Fe III, are formed and the same situation arise again. This is illustrated in Figure 2.3 where the EW of two iron lines, one neutral and one ionized, are plotted against  $T_{\text{eff}}$ . These two lines have similar EW in the Sun: 46.2 mÅ and 53.9 mÅ for the Fe I and Fe II line respectively.

### 2.2.3.2 Pressure dependence

Pressure dependence in the stellar atmosphere can be related to the gravity dependence. There are many ways to measure the pressure, and thus the gravity which is what is ultimately the goal with the measurement of  $\log g$ . Below are listed some of the most common methods to measure  $\log g$  from spectroscopy.

- Continuum: The Balmer jump is the only continuum feature sensitive enough to estimate the  $\log g$ .
- Hydrogen lines: Hydrogen profiles are pressure sensitive and can therefore be used to estimate  $\log g$ . However, the gravity dependence rapidly diminishes for temperatures above 10 000 K.
- Other strong lines: There exists other strong lines with pressure-broadened wings such as the Ca II H and K lines. These are better for cooler stars than the hydrogen lines described above.

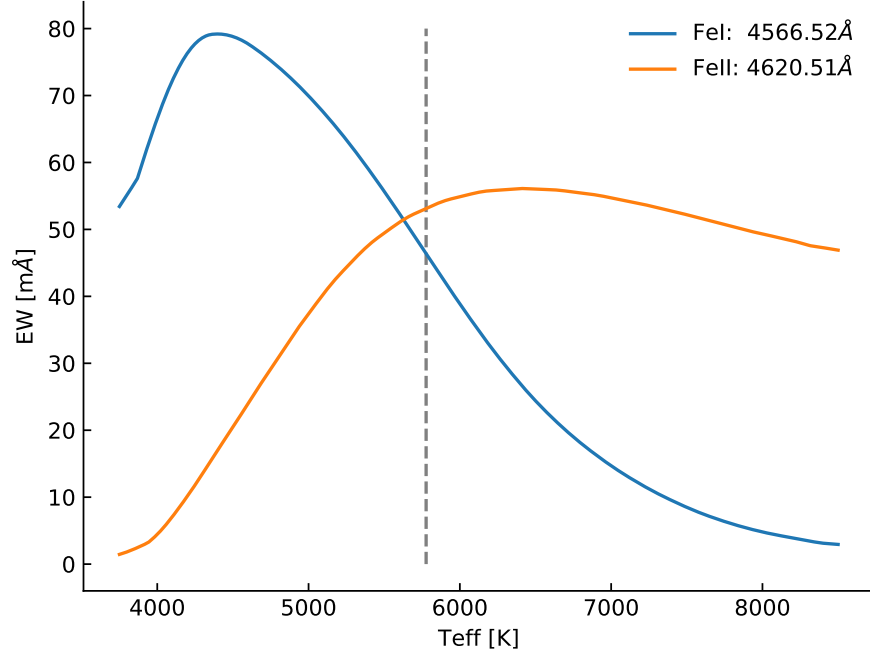


Figure 2.3: The EW for a Fe I and Fe II line with increasing  $T_{\text{eff}}$ . The two lines have similar EW in the Sun and are found in the optical part of the spectrum. The vertical line show the solar  $T_{\text{eff}}$ .

- Weak lines: By comparing two stages of ionization for the same element it is possible to obtain  $\log g$  using weaker or modestly strong lines.

In this thesis weak lines are used to measure  $\log g$ . More specifically a comparison between Fe I and Fe II lines are used. For FGK stars, as the atmosphere contracts (i.e.  $\log g$  increases) the pressure likewise increases, which in turn means that both the gas pressure,  $P_g$ , and electron pressure,  $P_e$ , increases. Since hydrogen is the main electron contributor, but not fully ionized for these stars, the electron pressure is much smaller than the gas pressure. The gas pressure follow a simply empirical approximation with gravity:

$$P_g \approx \text{constant } g^{2/3}, \quad (2.8)$$

where  $g$  is the gravity. The electron pressure is given by

$$P_e \approx \text{constant } g^{1/3}. \quad (2.9)$$

There are three cases for which a line show dependence on gravity, when considering only weak lines:

1. A weak line formed by any ion or atom, where most of the element is in the next higher ionized state.
2. A weak line formed by any ion or atom, where most of the element is in the same ionized state.

3. A weak line formed by any ion, where most of the element is in the next lower ionized state.

Using the Saha equation for case 1, it is important to note that the number of the atoms in the highest state is roughly equal to the total number of atoms of that element,  $N_{r+1} \approx N$ . Hence

$$N_r \approx \text{constant } P_e \quad (2.10)$$

which means that the line absorption coefficient is

$$l_\nu \approx \text{constant } N_r \approx \text{constant } P_e. \quad (2.11)$$

The strength of a weak line,  $R$ , is proportional to the ratio of the line to the continuous absorption coefficient,  $\kappa_\nu$

$$R = \frac{F_c - F_\lambda}{F_c} = \text{constant } \frac{l_\nu}{\kappa_\nu}. \quad (2.12)$$

When negative hydrogen dominates  $\kappa_\nu$  which is the case here it is proportional to the electron pressure,  $\kappa_\nu \propto P_e$  which means the line strength is not proportional to electron pressure:

$$R = \frac{l_\nu}{\kappa_\nu} \approx \text{constant}. \quad (2.13)$$

For case 2, the approach is the same, here  $N_r \approx N_{r+1} \approx N = \text{constant}$ . This leads to  $l_\nu \approx \text{constant}$ , eventually giving

$$R = \frac{l_\nu}{\kappa_\nu} \approx \frac{\text{constant}}{P_e} \approx \text{constant } g^{-1/3}. \quad (2.14)$$

Only the first two cases are relevant for solar-type stars used in this thesis, and the relation for the third case will be omitted.

In Figure 2.4 is shown how the Fe II line used previously change with  $\log g$ . The curve of growth is shown in the upper panel, while a synthetic spectrum for each  $\log g$  is presented in the lower left panel. It is clear that the ionized line is sensitive to  $\log g$  as shown in the lower right panel, where the correlation between the abundance and  $\log g$  is 0.40. This is expected as can be seen in Gray (2005, Table 16.1). There is used  $\delta \log A / \delta \log g$  as an indicator, and for neutral elements the correlation is much weaker. It is important to note that the correlation does change with  $T_{\text{eff}}$  and the element used.

### 2.2.3.3 Abundance dependence

The abundance of a given element obviously has an effect on the EW. The more abundant an element is, the more photons can be absorbed thus increasing the EW. However, the relationship is not strictly linear. For weak lines (GIVE RANGE) EW is approximately linear with the abundance, however it reach a plateau where the core of the line saturates. In this regime the EW only increases slowly, until the absorption "spills" into the wings and the increase is again linear. However, for these strong lines the profile is no longer Gaussian. The curve of growth for the same Fe I line used in Figure 2.3 is shown in Figure 2.5. Instead of EW it is common to use the reduced EW,  $\log(EW/\lambda)^1$ , which we will use more

<sup>1</sup> The reduced EW is useful since it normalises Doppler-dependent phenomena, such as microturbulence and thermal broadening.

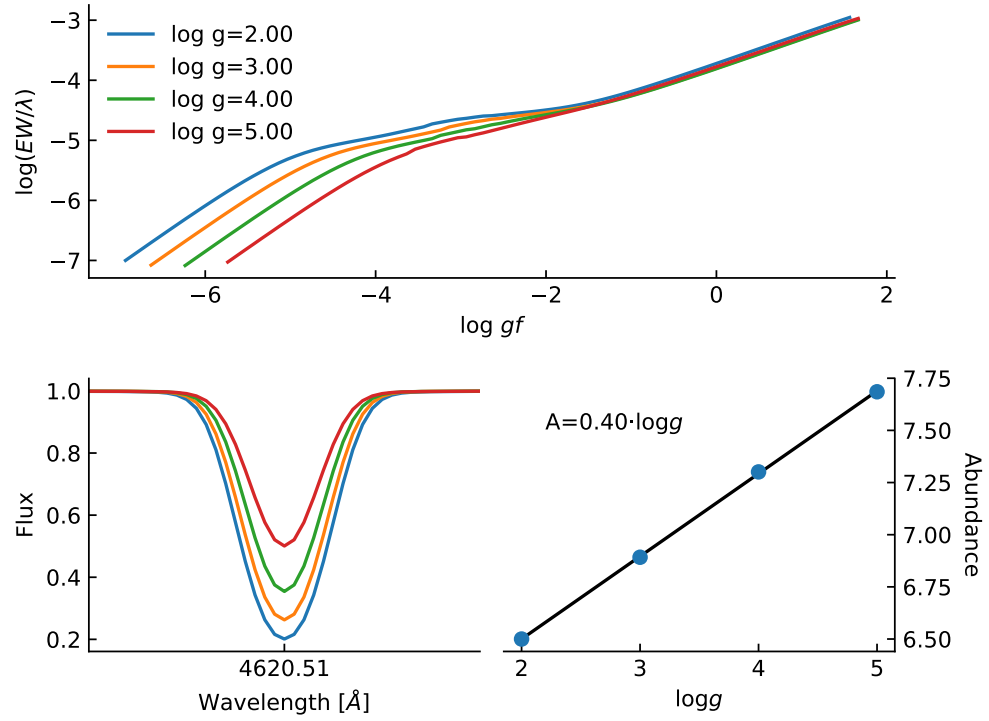


Figure 2.4: *Upper panel:* Curve of growth for same Fe II used in Figure 2.3 for four different  $\log g$  values. Here it is the weak lines mostly affected by the change in  $\log g$ . *Lower left panel:* Synthetic spectra of the same line. The colour scale is the same. *Lower right:* The abundance for the line at different  $\log g$ . A strong correlation (0.40) is seen.

later. Instead of the abundance of a line, the oscillator strength,  $\log gf$ , is used.

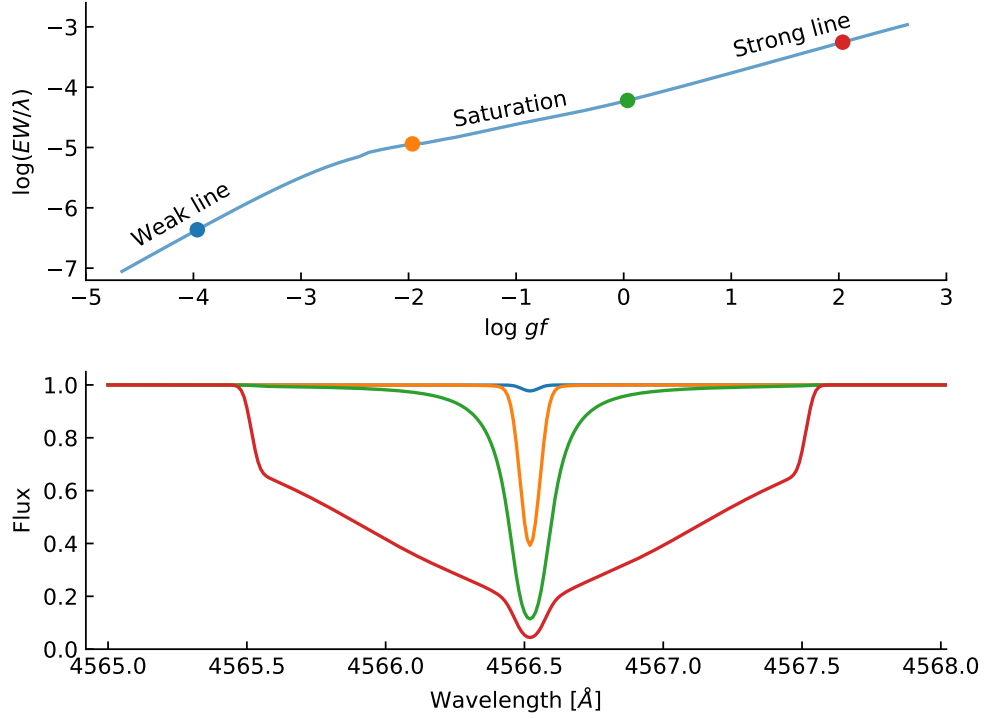


Figure 2.5: *Upper panel:* Curve of growth of the same Fe I line as used in Figure 2.3. Four points are marked which is shown in the *lower panel* as a synthetic spectral line. The RW (proxy for EW) is clearly increasing with  $\log gf$  (proxy for abundance).

#### 2.2.3.4 Microturbulence

Small-scale motion, that is motion of material at length scales small compared to the unit optical depth, are called microturbulence,  $\xi_{\text{micro}}$ . This is not to be confused with macroturbulence, which is motion of material at scales larger than the unit optical depth. The latter is associated with granulation and will not be discussed further in this thesis.  $\xi_{\text{micro}}$  comes into play when looking at the curve of growth for saturated lines (i.e. between green and red points in Figure 2.5). If no  $\xi_{\text{micro}}$  is assumed, then the measured abundance is higher than predicted by models based on thermal and damping broadening alone. In Figure 2.6 is shown three curves of growth with  $\xi_{\text{micro}} = 0.5 \text{ km/s}, 2.5 \text{ km/s}, 5.0 \text{ km/s}$ . As  $\xi_{\text{micro}}$  increases, so does the EW and hence the abundance.

The broadening of an absorption line measured by the shift in wavelength,  $\Delta\lambda$ , when  $\xi_{\text{micro}}$  is included is defined as:

$$\Delta\lambda = \frac{\lambda_0}{c} \sqrt{\frac{2kT}{m} + \xi_{\text{micro}}^2}, \quad (2.15)$$

where  $c$  is the speed of light,  $\lambda_0$  is the rest wavelength of the given line,  $k$  is Boltzmann's constant,  $T$  is the temperature, and  $m$  is the mass of the atom. Setting  $\xi_{\text{micro}} = 0 \text{ km/s}$ , we end up with thermal broadening.

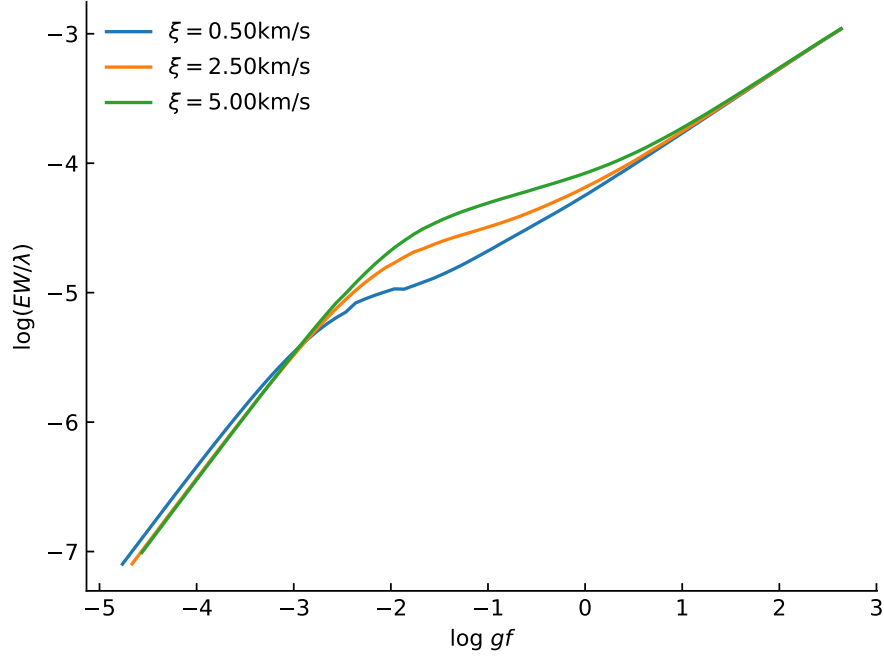


Figure 2.6: Curve of growth for three different values of  $\xi_{\text{micro}}$ . The EW is increasing with increasing  $\xi_{\text{micro}}$ .

## 2.3 Line list and atomic data

As mentioned above, the atomic data of the absorption lines are required. These data can be found in a database such as *The Vienna Atomic Line Data Base* (VALD) (Kupka et al., 2000; Piskunov et al., 1995). For compiling a usable iron line list, all theoretical transitions in a given wavelength range are requested from VALD. In the near-infrared (NIR), YJHK bands, there are several thousands of theoretical transitions.

In this thesis the EWs are measured (see Section 3.3.2) for all these lines using a solar spectrum (Hinkle et al., 1995, is used here). Here there are four possible outcomes. 1) A line can not be measured and is thus discarded, 2) the EW of the line is weak (below 5 mÅ) to be reliable, 3) the EW of the line is too strong (above 150 mÅ) and the line show non-linear behaviour in the curve-of-growth (see Figure 2.5), or 4) the EW of the line is between the two limits and is then added to the final line list.

After removing lines which EW is outside the range of EW mentioned above, it is good practise to have a visual inspection. Here one should look for severe line blending with other absorption lines which might prove problematic and unreliable measurements of the EW. If the reference spectrum used, here for the Sun, is not corrected for telluric lines, it is also a good idea to remove lines which exists amidst forest of telluric lines, as these absorption lines might fall on the telluric lines, if the star observed has a different radial velocity (RV).

When blended lines and otherwise lines which shows strange features (can be in a forest of telluric lines), the last step is to calibrate the atomic data. As mentioned above, this is done by changing the  $\log gf$  value for a given line, until it has the desired determined abundance. In this case, an iron line

should have the abundance of 7.47 using the values from [Gonzalez and Laws \(2000\)](#), when using a solar atmosphere model. There is a simple anti-correlation between the determined abundance from the measured EW and the  $\log gf$ , so a simple bisector minimization can be used to find the best  $\log gf$ . It is important to calibrate the  $\log gf$  when changing the version of MOOG (or if other radiative transfer codes are used), the atmosphere model and version of those, and even the interpolation of the atmosphere models. These changes in  $\log gf$  should be minor compared to the change from the VALD database and those we arrive at when calibrated for the Sun.

## 2.4 Spectrographs

This chapter will be focused on some of the available spectrographs for deriving stellar atmospheric parameters using the method described in Section 3.3. For this we need a spectrum of both high resolution and high signal-to-noise ratio, S/N, which combined will be called a high quality spectrum. In order to get reliable results, a spectral resolution of at least  $R = \frac{\lambda}{\Delta\lambda} = 25\,000$  is needed. A  $S/N \approx 100$  is at least needed to obtain the parameters. These are approximately values since it can vary across different spectral classes, e.g. it is often relatively easy to obtain parameters of a solar-twin while it gets increasingly difficult as especially  $T_{\text{eff}}$  diverges in either direction from the solar value. Naturally the higher quality the spectrum is (both resolution and S/N), the better the results will be obtained. It is common practise to increase the S/N for a spectrum by co-adding a sample of lower S/N spectra of the same star from the same spectrograph. This is often used if the star of interest is so dim that it takes several observations to reach a sufficient high S/N. Another case is when spectra have been obtained from the archive. The scientific goal can be very different, e.g. obtaining radial velocities (RV) where a much lower S/N is needed, however here numerous spectra are needed. It is common to search for exoplanets with the RV detection method, where multiple spectra are obtained, and the stellar parameters are then obtained after co-adding the multiple spectra. It is of course important to put the spectra on a common RV, usually at 0 km/s.

Spectrographs work in different wavelength regions. The most used region is the optical part of the spectrum, which is also ideal for studying FGK stars with relative low line blending and low telluric contamination. In the recent years there has been an increase of NIR spectrographs. These will mainly be used to study the distant Universe, i.e. at high red-shifts, and cool objects in our own galaxy. Especially interesting are the M stars which consist of around 70% of all stars in our galaxy ([Bochanski et al., 2010](#)). These stars are intrinsic dim because of their low  $T_{\text{eff}}$ , ranging from 2200 K to 3500 K, hence most of their light emitted will be in the NIR. It is advantageous to collect as much light as possible from these dim stars, since reaching a similar S/N in the optical would be more time expensive. The cool M stars have more molecules in the atmosphere than their hotter counterparts. This can be seen in the spectrum, where molecular lines greatly depress the continuum (and me), making EW measurements difficult. This continuum depression is much larger in the optical than the NIR, giving another motivation for studying stars in this wavelength region.

Remove stupid  
joke!



## Chapter 3

# Deriving stellar parameters

There are different methods for obtaining stellar atmospheric parameters. Here follows a short description of some of the most common methods, however the spectroscopic method will be explained in much greater detail later in this chapter.

### 3.1 Photometry

Photometry can be used in different ways to estimate the effective temperature. In this section two methods will be mentioned; a colour calibration, and asteroseismology. There are other methods, e.g. SED fitting but this will not be discussed further.

#### 3.1.1 InfraRed Flux Method - IRFM

The InfraRed Flux Method (IRFM) was first described by [Blackwell and Shallis \(1977\)](#). From IRFM it is possible to measure the stellar radius and  $T_{\text{eff}}$  with a measurement of the angular diameter,  $\theta$ , derived from infrared photometry.  $T_{\text{eff}}$  is derived from the angular diameter from the simple relation

$$\sigma T_{\text{eff}}^4 = \frac{4\mathcal{F}_E}{\theta^2}, \quad (3.1)$$

where  $\mathcal{F}_E$  is the monochromatic flux measured at Earth, and  $\sigma$  is Boltzmann's constant. The angular diameter is calculated from the following equation:

$$\theta = 2\sqrt{\mathcal{F}_E/\mathcal{F}_S}, \quad (3.2)$$

where  $\mathcal{F}_S$  is the calculated monochromatic flux from the star. This flux is based on a model atmosphere with an effective temperature based on the spectral energy distribution (SED). The calculated flux show a strong dependence on  $T_{\text{eff}}$  in the visible, however this dependence is much weaker in the infrared. Hence a poor first estimation of  $T_{\text{eff}}$  will lead to a reliable angular diameter. From this new angular diameter  $T_{\text{eff}}$  can be re-derived, a new model atmosphere can be used with a new set of  $\mathcal{F}_S$  can be calculated. Iteratively the angular diameter and  $T_{\text{eff}}$  can be calculated. If the distance  $d$  is known of the star, the stellar radius is  $R_* = \frac{\theta d}{2}$ . The solar flux, both measured and calculated, from [Blackwell and Shallis \(1977\)](#) are shown in Figure 3.1. Using the data provided the solar radius and  $T_{\text{eff}}$  were derived using the

equations above:  $R = 1.011R_{\odot}$  and  $T_{\text{eff}} = 5963 \text{ K}$ . This was simply done for each wavelength, and the results presented here are just a simple average value.

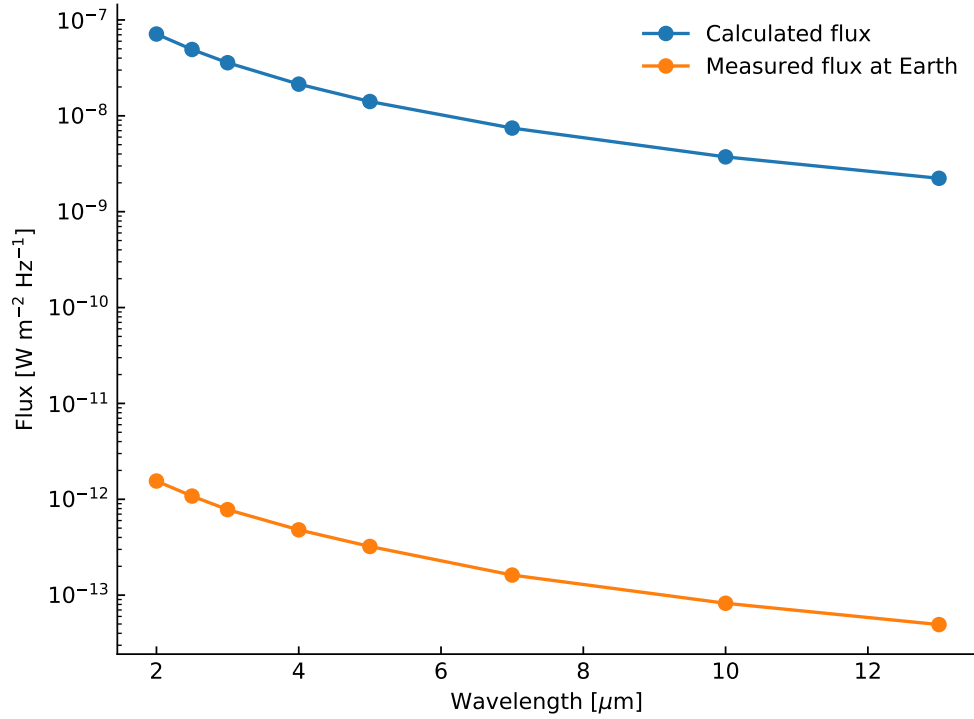


Figure 3.1: Measured and calculated flux from the Sun at infrared wavelengths. Data from Table 2 in [Blackwell and Shallis \(1977\)](#). Mean solar radius from this data is  $1.011R_{\odot}$ , and mean solar  $T_{\text{eff}} = 5963 \text{ K}$  using Equation 3.1.

The main drawbacks of the IRFM is the model dependence, a drawback many methods share, and the need of high precision infrared photometry. For the model atmosphere a metallicity and surface gravity is assumed which has an effect on  $\mathcal{F}_S$ , and hence on the final derived  $T_{\text{eff}}$  and  $R$ . A more in-depth description of the IRFM can be seen in e.g. [Casagrande et al. \(2006, section 4\)](#).

### 3.1.2 $T_{\text{eff}}$ -colour-[Fe/H] calibration

Photometry can be used for deriving  $T_{\text{eff}}$  using existing colour calibrations like that of for example [Ramírez and Meléndez \(2005b\)](#) where adopted  $T_{\text{eff}}$  and [Fe/H] in combination with colours such as  $B - V$ ,  $V - S$ , etc. are used to fit a polynomial such that the  $T_{\text{eff}}$  can easily be estimated with a simple relation:

$$T_{\text{eff}} = \frac{5040}{\theta_{\text{eff}}} + P(X, [\text{Fe}/\text{H}]), \quad (3.3)$$

where

$$\theta_{\text{eff}} = \frac{5040}{T_{\text{eff}}} \quad (3.4)$$

$$= a_0 + a_1 X + a_2 X^2 + a_3 X[\text{Fe}/\text{H}] + a_4 [\text{Fe}/\text{H}] + a_5 [\text{Fe}/\text{H}]^2 \quad (3.5)$$

is the polynomial fit between  $T_{\text{eff}}$  versus a colour ( $X$ ) and the metallicity. The polynomial  $P(X, [\text{Fe}/\text{H}])$  is a correction applied to remove trends in the residuals, for example spectral features such as the Balmer lines or the Paschen jump. This correction is performed after the initial fit.

After obtaining the coefficients ( $a_i$ ) for different combinations of colours, it is trivial to obtain  $T_{\text{eff}}$  if the metallicity and a colour is known of the star.

### 3.1.3 Asteroseismology

Asteroseismology is the study of stellar pulsations. These pulsations propagate as sound waves throughout a star, their origin and amplitude is determined by the characteristics of the star, hence the study of the pulsations, which are seen on the surface, will thus be a study of the stellar properties. In order to study these a time series is needed. This can both be radial velocities as it was used in the recent results from the SONG telescope (Grundahl et al., 2017), or photometry like the numerous results from e.g. the space telescopes *CoRoT* and *Kepler* (see e.g. Chaplin et al., 2011; Christensen-Dalsgaard et al., 2010; Huber et al., 2014). The analysis is identical for either time series, however the amplitudes in the power spectrum will look different.

After determining the frequencies of a range of pulsations from a power spectrum of the time series, a pattern emerge at every  $\Delta\nu$  (the so-called large frequency separation). A finer pattern also occur described by  $\delta\nu$ . Last the frequency at maximum power is also measured from the power spectrum,  $\nu_{\text{max}}$ . These frequency separations are used to obtain  $\log g$  via

$$\nu_{\text{max}} \propto \frac{g}{\sqrt{T_{\text{eff}}}} \quad (3.6)$$

$$= \frac{M/M_{\odot}}{(R/R_{\odot})^2 \sqrt{T_{\text{eff}}/5777}} 3.05 \text{ mHz}, \quad (3.7)$$

where  $\nu_{\text{max},\odot} = 3.05 \text{ mHz}$  is the frequency of maximum amplitude for the Sun. A similar equation exists for the determination of the stellar density:

$$\Delta\nu = (M/M_{\odot})^{-1/2} (R/R_{\odot})^{-3/2} 134.9 \text{ } \mu\text{Hz}. \quad (3.8)$$

These simple scaling relation are described in detail in Kjeldsen and Bedding (1995). These two equations can be used together to determine the mass and radius of the star, often to a high precision. These scaling relations are applicable for stars which shows solar-like oscillations, mostly found in main sequence FGK stars, but can also be found in red giant stars. The mass and radius for a range of  $\nu_{\text{max}}$  and  $\Delta\nu$  can be seen in Figure 3.2, where  $T_{\text{eff}} = 5777 \text{ K}$ . The star located at  $\{\Delta\nu = 134.9 \text{ } \mu\text{Hz}; \nu_{\text{max}} = 3.05 \text{ mHz}\}$  is the Sun.

The small frequency separation,  $\delta\nu$ , is sensitive to the sound-speed gradient in the core which in turn is sensitive to the composition. Thus the small frequency separation is a very important diagnostic for stellar evolution. An interesting case is that of Bedding et al. (2011), where it was shown it is possible to distinguish between hydrogen- and helium-burning cores in red giant stars.

A drawback of asteroseismology is the dependence of  $T_{\text{eff}}$  in Equation 3.7 which has to be provided from another method. Ideally this will come from spectroscopy for which the determination of  $T_{\text{eff}}$  is often reliable. This drawback is minor compared to the lack of model dependence which is one of the strongest advantages of asteroseismology.

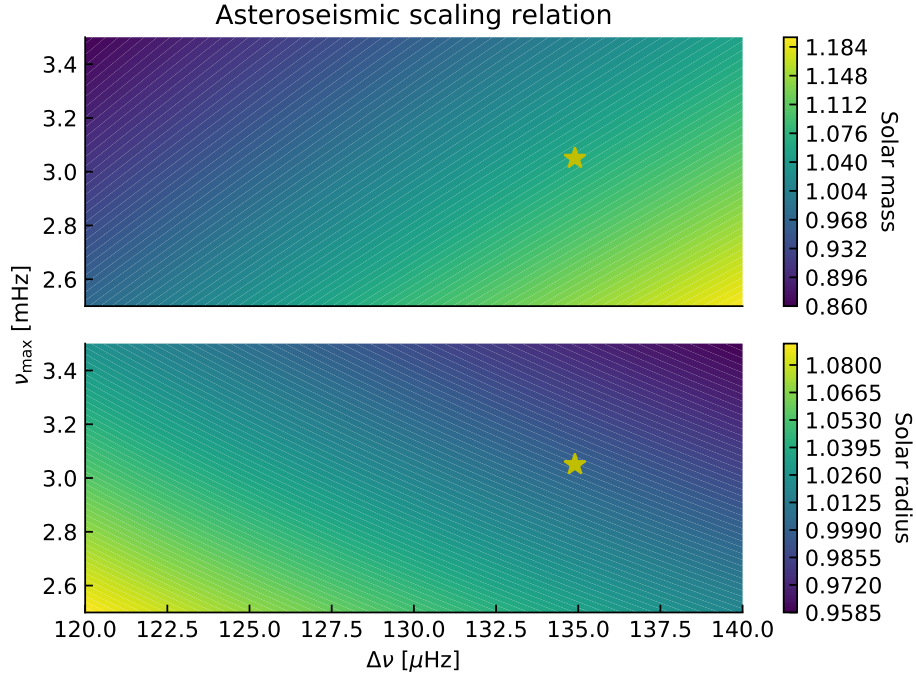


Figure 3.2: Mass and radius from asteroseismic scaling relation. The colour is the mass and radius for the upper and lower panel, respectively.

For both of the mentioned photometric methods to determine some atmospheric parameters a disadvantage is the dependence on the knowledge of other atmospheric parameters which usually comes from spectroscopy (e.g. metallicity). However, as will be discussed in Section 3.2  $\log g$  is often difficult to determine reliably and synergies are welcomed between different methods.

## 3.2 Spectroscopy

A spectrum can be analysed with a range of different methods. The method finally chosen depend on quality of the spectrum, i.e. high/low resolution and high/low S/N, the spectral type of the star, the region that was observed, e.g. UV, optical, NIR, etc., some stellar properties, e.g. fast-rotator, activity, etc. No methods work for all cases, but sometime several methods can be used for on case.

Since this thesis is focused on FGKM stars, and mainly dwarfs, three methods will be described; synthesis, spectral indices, and the EW method. The latter method will be described in a separate section since this is the main method used for the analysis in this thesis.

### 3.2.1 Synthesis

The synthesis fitting method is a standard method for obtaining stellar atmospheric parameters from a wide range of spectra, that is with different spectral resolution, spectral parameters such as  $T_{\text{eff}}$ ,  $\log g$ ,  $v \sin i$  the projected rotational velocity, etc., and S/N (see e.g. Tsantaki et al., 2017). The synthetic fitting method is in simple terms a comparison between the observed spectrum and a synthetic spectrum,

which is either calculated on the fly like Spectroscopy Made Easy (SME) (Valenti and Piskunov, 1996), or using a pre-calculated grid like Starfish (Czekala et al., 2015). By analysing the

$$\chi^2 = \sum_i^N \frac{(y_{\text{obs},i} - y_{\text{model},i})^2}{\sigma_i}, \quad (3.9)$$

the synthetic spectrum that best match the observed spectrum can be found. Here the  $y_{\text{obs}}$  is the observed spectrum,  $y_{\text{model}}$  is the synthetic spectrum, and  $\sigma$  is the error on the measurement.

The synthetic fitting can be done by utilising small windows around sensitive spectral features such as ionized lines or hydrogen lines for obtaining the surface gravity, iron lines for obtaining the effective temperature, a series of different atomic lines for obtaining the overall metallicity. This approach is used by FASMA and SME (Tsantaki et al., 2017; Valenti and Piskunov, 1996, respectively) and is a compromise between fitting the entire spectral range and calculating the synthetic spectra on the fly which is time consuming. On the other hand the entire spectrum can be fitted if a pre-calculated grid of synthetic spectra are available. By masking small windows, one can also exclude different features that are troublesome, this can be telluric lines, bad reduction of the spectra, or real spectral features where there currently is poor atomic/molecular data such as the oscillator strength and thus it is not possible to reliably fit this feature.

This method is affected by the different approaches one can use, that is which atmosphere models are used (ATLAS, MARCS, etc.), atomic data and whether this has been calibrated, the radiative transfer code in the case the synthetic spectra are calculated on the fly, and the minimization procedure chosen. With these things in mind it is important to stress the wide range spectra and spectral classes this method works with.

### 3.3 FASMA

The EW method or curve-of-growth analysis is another standard method for obtaining stellar atmospheric parameters from spectra as the synthetic fitting method (Section 3.2.1). Since this is the method used throughout this thesis it will be explained in detail. This analysis follow a chain of tasks, each has been made automatic in the software Fast Analysis of Spectra Made Automatically (FASMA<sup>1</sup>) which was developed during this thesis (Andreasen et al., 2017b). FASMA is made of three `drivers`:

1. EW measurement driver
2. Obtain stellar atmospheric parameters driver
3. Abundance driver

An additional driver is under development; a synthetic fitting driver (Tsantaki et al., 2017). FASMA has been made available to the community via a web application at <http://www.iastro.pt/fasma/>.

#### 3.3.1 Ingredients

FASMA is written in the Python programming language and glue together other software and model atmospheres necessary for obtaining stellar atmospheric parameters from high quality spectra. These

---

<sup>1</sup> Greek for spectrum

software and models are described in greater detail in the following sections. In short, the curve-of-growth analysis require measured EWs where the latest version<sup>2</sup> of **ARES** is used (Sousa et al., 2015). These EWs are used to derive line abundances using model atmosphere like the ATLAS9 (Kurucz, 1993), MARCS models (Gustafsson et al., 2008), or PHOENIX models (Husser et al., 2013) to mention the most popular for this analysis. Note that the PHOENIX models are relative new and not as widely used yet. In tandem with model atmospheres a radiative transfer code is also needed. **FASMA** uses **MOOG** (Snedden, 1973) for this. The model atmosphere usually comes in a pre-calculated grid in the  $\{T_{\text{eff}}, \log g, [\text{Fe}/\text{H}]\}$  parameter space. These are interpolated in order to access the requested combination of parameters. Last, **FASMA** consist of a minimization routine which looks for the best matching parameters given a spectrum.

### 3.3.2 Wrapper for ARES

There are two ways to measure the EW of an absorption line, manually or automatically. There are advantages and disadvantages for both method. For the manual, an advantage is that we can inspect the lines and try to measure lines in different ways (which is useful if it is blended). We have more control over how blended lines are fitted, and which profiles are used. Disadvantages are that it is very time consuming, and it is prone to errors, as a measurement might change drastically by the eyes measuring it. Even for the same person, the measurement can change. By mentioning the advantages and disadvantages of the manual method, it should be clear that the advantages and disadvantages of the automatic method is the opposite of those. Especially the time to measure the lines are orders of magnitudes faster, which is crucial when dealing with more than a handful of spectra.

When a line is measurement by hand (manually) it is in this thesis done using the `splot` command in **IRAF**. Here the deblending mode is used whenever necessary. It is often necessary to fit one spectral lines with several Gaussians, as neighbouring lines might contaminate the line of interest.

When a line is measurement automatically it is in this thesis done with **ARES** (Sousa et al., 2015, 2007). When using **ARES** it is important to use a correct value of the `rejt` parameter. This parameter is used for placing the continuum level, and is thus directly related to the final measurement EW. It is difficult to get this parameter right, however the newest version of **ARES** has the option to analyse a few absorption free regions and measure the S/N. The `rejt` is then calculated as:

$$\text{rejt} = 1 - \frac{1}{\text{S/N}}.$$

**ARES** is used via the first driver of **FASMA**. All the options available for **ARES** can be accessed by **FASMA**. The options are

- Setting the spectral window,  $\lambda_{\text{min}}$  and  $\lambda_{\text{max}}$
- RV correction to be applied or a mask to measure the RV and automatic make this correction
- minimum and maximum EW to be considered (5 mÅ and 150 mÅ respectively by default)
- Minimum distance between two consecutive lines
- Smoothing applied with a `boxcar` filter before measuring the EWs

<sup>2</sup> The latest version can be found here: <https://github.com/sousasag/ARES>

An in-depth description of these options can be found in [Sousa et al. \(2015, 2007\)](#).

Sometimes **ARES** crash when measuring an absorption line. The reason is not clear, however when dealing with a large amount of spectra, it is important that the analysis moves on. To deal with this problem, **FASMA** finds the last line which **ARES** tried to measure in the log file. This line is temporarily removed from the line list and **ARES** is restarted. The line list used for deriving parameters consists of numerous iron lines, thus removing one line will have a negligible effect on the final derived parameters.

### 3.3.3 Interpolation of atmosphere models

**FASMA** has access to both ATLAS9 models by [Kurucz \(1993\)](#) and MARCS models by [Gustafsson et al. \(2008\)](#), both are in a pre-calculated grid as described above. Let this grid be described by  $\{T_{\text{eff},g}, \log g_g, [\text{Fe}/\text{H}]_g\}$ , where subscript  $g$  is one of the grid points. Such a grid can be seen in [Figure 3.3](#) for  $[\text{Fe}/\text{H}] = 0.00$  in the  $T_{\text{eff}}$  range; 3000 K to 10 000 K. For visualisation the location of the Sun is shown as well. The colour scale corresponds to the temperature in the first layer of each model atmosphere, i.e. the uppermost layer. The requested value will be  $\{T_{\text{eff},r}, \log g_r, [\text{Fe}/\text{H}]_r\}$ . The task is now to find the surrounding grid points in the parameter space of the requested parameters. For  $\log g$  and  $[\text{Fe}/\text{H}]$  two neighbouring grid point are used, and for  $T_{\text{eff}}$  four surrounding grid point are used, in total  $4 \times 2 \times 2 = 16$  model atmospheres for the interpolation. **FASMA** use the four surrounding grid points for  $T_{\text{eff}}$  instead of two, since the model atmosphere changes most with  $T_{\text{eff}}$ . This is common in other interpolations as well (see e.g. [Valenti and Piskunov, 1996](#)).

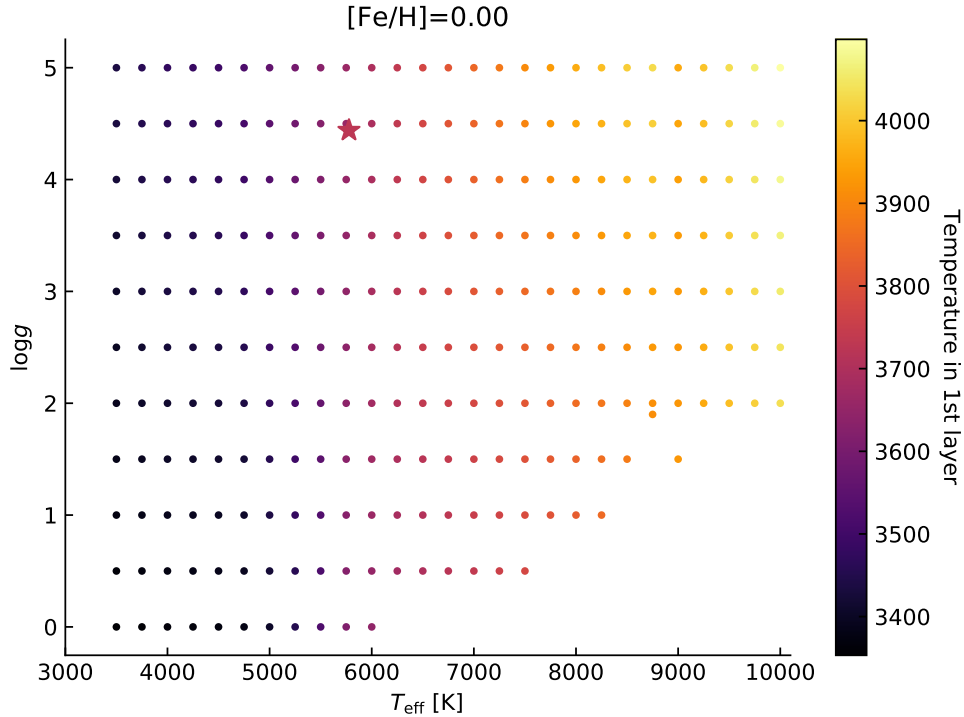


Figure 3.3: Model atmosphere grid from [Kurucz \(1993\)](#) at  $[\text{Fe}/\text{H}] = 0.00$  between 3000 K and 10 000 K. The grid extends to higher  $T_{\text{eff}}$ , but these are not considered in this thesis.

When the 16 model atmosphere have been located, the interpolation goes through each layer of the

model atmosphere, where there typical are 72 layers, and each column of which there are six. The columns are described in Section 2.2.1. The interpolation are done using the `griddata` function from `SciPy`<sup>3</sup>. The interpolation is linear in the parameter space. After the interpolation, the result is saved to a file in the format expected by `MOOG`.

### 3.3.4 Minimization

With the measured EWs for all the lines in the line list, we choose an atmosphere model to determine the abundances. If there is no prior knowledge of the star it is common simply to choose an atmosphere model with solar parameters as a starting point. Once the line abundances of all the iron lines has been determined, the linear correlation between the abundances and the reduced EWs (RW), and the abundances and the excitation potential is calculated. If there is a correlation it means the model atmosphere used is wrong. Moreover, we also have to check if the mean abundance of Fe I and Fe II lines are equal, and last if mean abundance of the Fe I lines is equal to the input  $[M/H]$  of the atmosphere model<sup>4</sup>. If one of these four criteria does not pass, then the atmosphere model is wrong, and we have to search for a new one. A common way to do this, is by combining the indicators into a scalar value:

$$f(\{T_{\text{eff}}, \log g, [Fe/H], \xi_{\text{micro}}\}) = \sqrt{a_{\text{EP}}^2 + a_{\text{RW}}^2 + \Delta\text{Fe}^2}, \quad (3.10)$$

where  $a_{\text{EP}}$  is the correlation between abundances and excitation potential,  $a_{\text{RW}}$  is the correlation between abundances and RW, and  $\Delta\text{Fe}$  is the difference between the mean abundances of Fe I and Fe II. This scalar function can be minimized using standard minimization procedures as the simplex downhill among others. However, there is another approach that takes into the account the information stored in these indicators. For example, if  $a_{\text{EP}}$  is positive it means  $T_{\text{eff}}$  has to be increased by an amount correlated by the numerical value of  $a_{\text{EP}}$ . In the same way, a non-zero  $a_{\text{RW}}$  means  $\xi_{\text{micro}}$  has to be changed, and  $\Delta\text{Fe}$  is an indicator for  $\log g$ . In the end it is a vector function being minimized which are more difficult, however we are not minimizing this using standard mathematical methods, but rather using the physical knowledge. This minimization is useless for anything else, but it is excellent for this. The vector function has the form:

$$f(\{T_{\text{eff}}, \log g, [Fe/H], \xi_{\text{micro}}\}) = \{a_{\text{EP}}, a_{\text{RW}}, \Delta\text{Fe}, \text{Fe I}\}. \quad (3.11)$$

The abundances of Fe I lines versus EP and RW are shown in Figure 3.4 for the planet host star HATS-1. The three rows are for three different model atmospheres. From upper to lower:

- Converged:  $T_{\text{eff}} = 5959 \text{ K}$ ,  $\log g = 4.59$ ,  $[Fe/H] = -0.04$ , and  $\xi_{\text{micro}} = 1.05 \text{ km/s}$ .
- Converged with  $0.5 \text{ km/s}$  added to  $\xi_{\text{micro}}$ .
- Converged with  $500 \text{ K}$  added to  $T_{\text{eff}}$ .

Left column show the abundances against the EP, and the right column is abundances against RW.

The minimization with the different options is depicted in Figure 3.5. In each iteration where convergence is not reached, the input metallicity is changed to that of the average output metallicity

<sup>3</sup> <https://scipy.org/>

<sup>4</sup> We use Fe I instead of Fe II lines for this, since they are more numerous.



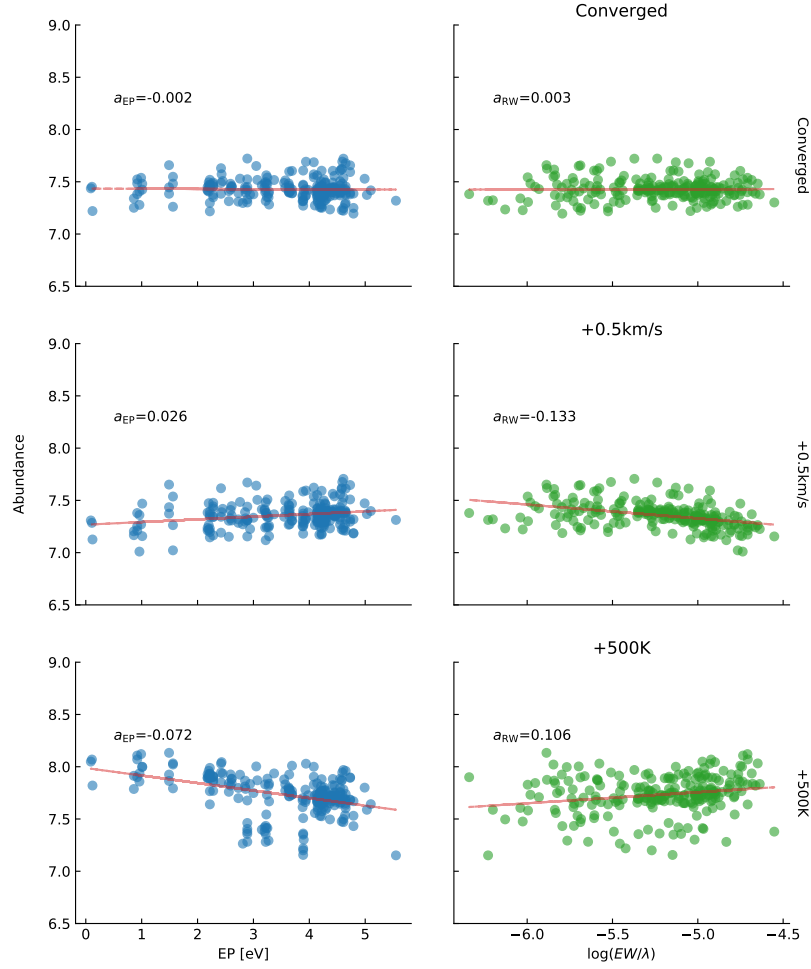


Figure 3.4: The abundances of FeI for the planet host star: HATS-1. Upper plot: Converged parameters (see text for stellar parameters for this star). Middle plot: Converged parameters with 0.5 km/s added to  $\xi_{\text{micro}}$ . Lower plot: Converged parameters with 500 K added to  $T_{\text{eff}}$ .

using the Fe I lines. **FASMA** is able to fix one or all of the four atmospheric parameters, and when it reach convergence it checks if there are any outliers in the abundances. These will be removed, either:

- All outliers above  $3\sigma$  once; minimization routine is restarted after removal of outliers.
- All outliers above  $3\sigma$  iteratively; minimization routine is restarted after removal of outliers each time.
- One outlier above  $3\sigma$  (with the highest deviation) is removed iteratively; minimization routine is restarted after removal of outliers each time.

All restarts of the minimization will start at the precious best found parameters. For the latter two were outliers are removed iteratively, this will continue until no outliers are present. An optical line list like the ones by [Sousa et al. \(2008\)](#); [Tsantaki et al. \(2013\)](#) have been tested thoroughly and it is safe to remove a larger amount of lines and still obtain reliable parameters, thus using the first option is common here. However, with a less tested line list, like the one by [Andreasen et al. \(2016\)](#) (and refined in [Andreasen et al. \(2017a\)](#)), one should remove outliers more carefully, and it is recommended that one outlier is removed iteratively.

Sometimes the minimization can not reach convergence with all parameters free. The first approach to progress is to fix  $\xi_{\text{micro}}$  to a value. This parameter is known to depend on the spectral type (see e.g. [Tsantaki et al., 2013](#), and references therein). **FASMA** use one of two empirical relations to fix  $\xi_{\text{micro}}$  if this is close to either 0km/s or 5km/s and  $|a_{\text{RW}}| > 0.050$  at the end of the minimization. The empirical relations are:

$$vt = \begin{cases} 6.935 \cdot 10^{-4} T_{\text{eff}} - 0.348 \log g - 1.437 & \text{For } \log g \geq 3.95 \\ 2.72 - 0.457 \log g + 0.072 \cdot [\text{Fe}/\text{H}] & \text{For } \log g < 3.95, \end{cases} \quad (3.12)$$

where the first case is from [Tsantaki et al. \(2013\)](#) and the latter case is from [Adibekyan et al. \(2015\)](#). In this way  $\xi_{\text{micro}}$  is changed in each iteration according to one of these relations. This option is called **autofixvt** in Figure 3.5.

Last there is an option, **refine**. This apply more strict criteria for the indicators to reach convergence, thus making the minimization less sensitive to the initial guess since it could otherwise reach convergence from one "side" of the parameter space. The default criteria are:

$$\begin{aligned} a_{\text{EP}} &= 0.001 \\ a_{\text{RW}} &= 0.003 \\ \Delta\text{Fe} &= 0.001. \end{aligned}$$

The criteria for  $a_{\text{RW}}$  is not as strict as  $a_{\text{EP}}$  since this indicator can change rapidly with small changes in  $\xi_{\text{micro}}$ , thus a very strict criteria might never lead to convergence. Convergence is reached once all of the above criteria are met, and the input and output metallicity are identical. If one or more of the parameters are fixed, the corresponding criterion is simply set to 0 and effectively ignored, thus not changing the parameter.

For each iteration, the change to be applied for the atmospheric parameters are defined by adding the

following:

$$T_{\text{eff}} : 2000 \text{ K} \cdot a_{\text{EP}} \quad (3.13)$$

$$\xi_{\text{micro}} : 1.5 \text{ km/s} \cdot a_{\text{RW}} \quad (3.14)$$

$$\log g : -\Delta\text{Fe} \quad (3.15)$$

to each parameter. Note again that metallicity is simply changed to the the output metallicity of the previous iteration. These are empirical relations. Note that by changing e.g.  $T_{\text{eff}}$  not only is  $a_{\text{EP}}$  affected, but the other indicators as well as seen in Figure 3.4. This inter-dependency between the parameters is ignored by FASMA as it is not a simple problem to solve. The stepping presented above is chosen to rapidly reach convergence, without causing problems for the inter-dependency.

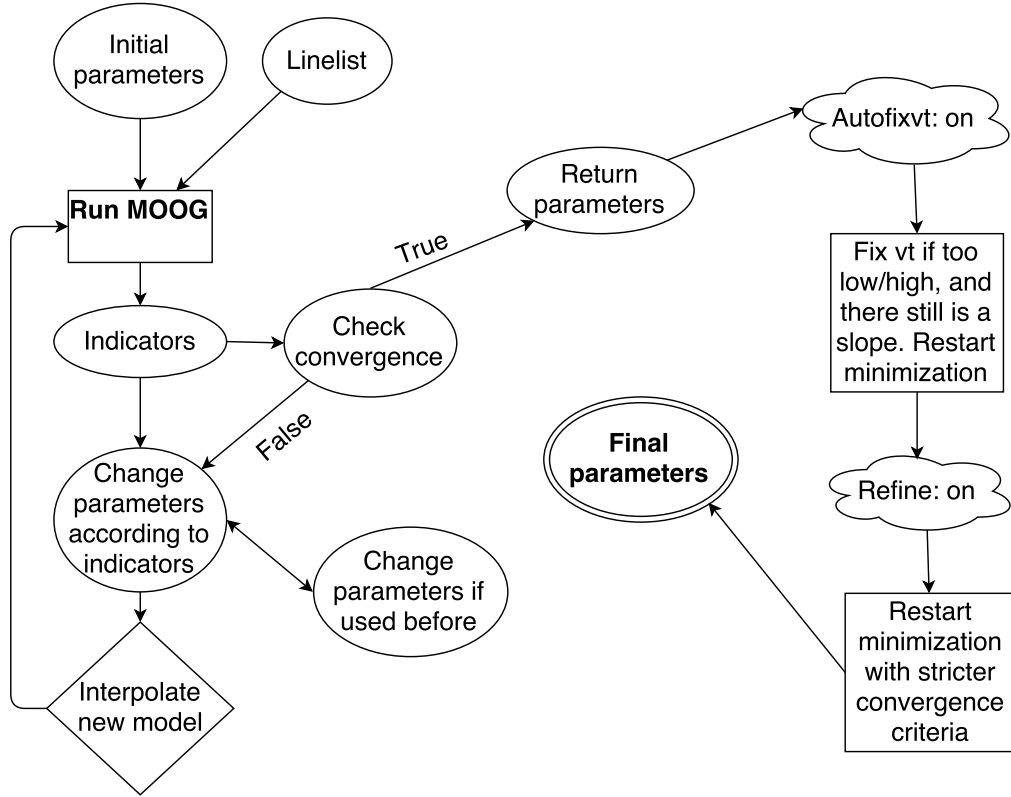


Figure 3.5: Overview of the minimization for FASMA . Credit: [Andreasen et al. \(2017b\)](#).

### 3.3.5 Error estimate

The error estimate is based on the same method presented in [Neuforge-Verheecke and Magain \(1997\)](#). The error on  $\xi_{\text{micro}}$  corresponds to the  $1\sigma$  statistical error on the slope of the linear regression between Fe I abundances and RW. The error on  $T_{\text{eff}}$  is the statistical error on the slope between Fe I abundances and EP as well as the uncertainty in  $\xi_{\text{micro}}$ . The error for  $[\text{Fe}/\text{H}]$  corresponds to the dispersion of the Fe I abundances as well as the uncertainties in  $\xi_{\text{micro}}$  and  $T_{\text{eff}}$ . The error in  $\log g$  corresponds to the dispersion in the pressure sensitive Fe II abundances.

# Chapter 4

## Results for FGK stars

Don't cry because it's over, smile because it happened.

Dr. Seuss

It is time to apply the theory and methodology on some data. In this chapter results from studies during the thesis will be presented. There is the analysis of three stars which lead to two papers, HD20010 (Andreasen et al., 2016) and Arcturus & 10 Leo (Andreasen et al., 2017a). Additionally, there was a analysis of how a cut in EP might affect the final parameters of a star. This will be discussed in Section 4.6, and last the analysis of a range of synthetic spectra from the PHOENIX spectral library (Husser et al., 2013), with  $T_{\text{eff}}$  lower than analysed in previous stars with the methodology described above in Section 3.3. However, before diving into the results of the analysis it is important to describe how the NIR line list were compiled and why and how it was later refined.

### 4.1 The creation of a NIR line list

As discussed extensively in Chapter 2 and Chapter 3, a atomic line list is needed for employing the method described here. This line list is made by iron lines in the NIR. This has already been mentioned in Chapter 2. Here the process will be explained in greater detail below for the two versions presented in Andreasen et al. (2016) and Andreasen et al. (2017b), respectively.

#### 4.1.1 First version

The first version of a NIR iron line list for determining stellar atmospheric parameters of high resolution and high S/N spectra were presented in Andreasen et al. (2016). Here all iron transitions between 10 000 Å to 25 000 Å<sup>1</sup> were downloaded from the VALD database (Kupka et al., 2000; Piskunov et al., 1995). This only includes Fe I and Fe II transitions. In total were 50 198 Fe I and 28 339 Fe II lines respectively from the VALD3 database.

The EW of all lines were measured in a solar atlas by Hinkle et al. (1995). The EWs were measured using ARES due to the large amount of lines and to be as consistent as possible in the measurements. Since ARES expect a 1D spectrum with equidistant wavelength step, the solar spectrum were interpolated

---

<sup>1</sup> That is equivalent to the YJHK bands.

onto a regular wavelength grid of  $0.01 \text{ \AA}$ . This did not change the appearance, and hence not the EW, of the final spectrum. This wavelength step is equivalent to a spectral resolution of 1 500 000 at  $15\,000 \text{ \AA}$ .

The EWs are measured by fitting Gaussian profiles to the spectral lines. For a given line, *ARES* output the central wavelength of the line (provided in the line list), the FWHM maximum of the fitted line, the number of lines fitted for the final result, the depth of the line, the EW of the line, and the Gaussian coefficients of the line. In the latest version of *ARES*, the error of the EW is also provided (Sousa et al., 2015). A few lines could not be measured by *ARES* and were simply discarded. It is not completely clear why *ARES* had troubles measuring these lines, however, since the amount was low (less than 1 per thousand) this was not a concern.

More lines were discarded according to the following criteria:

- Lines with EW lower than  $5 \text{ m\AA}$  as these lines can be problematic to see in spectra with lower S/N or spectra with many spectral features.
- Lines with EW higher than  $200 \text{ m\AA}$  as these lines are too strong to be fitted with a Gaussian profile. These lines might also be saturated and do not contain information about the abundance (see Figure 2.5).
- Lines where the total number of fitted lines are 10 or higher since they show indications of severe blending.
- If the fitted central wavelength is more than  $0.05 \text{ \AA}$  away from the wavelength provided by VALD3 to avoid false identification.

After this removal the number of Fe I and Fe II lines are reduced to 6060 and 2735, respectively.

#### 4.1.1.1 Visual removal of lines

At this point a visual inspection were necessary. All absorption lines from all elements were downloaded from the VALD3 database in a  $3 \text{ \AA}$  window around each of the nearly 9000 iron lines from the previous step. For each small spectral window, all absorption lines (including the iron line(s)) were plotted on top of the solar spectrum. An iron line were discarded if another line had the same central wavelength and/or the absorption line were severely blended. Most of the discarded iron lines had high EP, which are weak compared to the low EP lines. Therefore, it is fair to assume that many of these iron lines were falsely identified as another stronger line from another element. After the visual removal the number of Fe I and Fe II lines were reduced to a mere 593 and 22, respectively.

For some of the absorption lines it was not clear which element was the cause. These lines were marked for further investigation with synthesis as described below.

#### 4.1.1.2 Synthetic investigation

For the lines marked above for further investigation an even broader window were used of  $6 \text{ \AA}$ . Once again, all lines were downloaded from the VALD3 database in these spectral windows. *MOOG* were used with the *synth* driver to create a synthetic spectrum using a solar atmosphere model with  $T_{\text{eff}} = 5777 \text{ K}$ ,  $\log g = 4.438$ ,  $A(\text{Fe}) = 7.47$ , and  $\xi_{\text{micro}} = 1.00 \text{ km/s}$ . The iron abundance (7.47) is from Gonzalez and Laws (2000). The overall metallicity for the solar atmosphere model is  $[M/H] = 0.00$  by definition. This was done for all spectral windows for three different  $A(\text{Fe}) = \{-0.2, 0.0, 0.2\}$ . Before creating a synthetic

spectrum all elements which are more than singly ionised were removed since MOOG does not allow these. An example of this can be seen in Figure ??.

If the three synthetic spectra shows variation at the iron line of interest, then it is assumed that the iron line is the cause for the absorption line. As a simple test, the iron line was also removed from the line list used to create the synthetic spectra. If the iron line in the synthetic spectra disappeared, it was a clear signal that this line can be used in the final iron line list. In some cases two iron lines had the same or very similar wavelength, and this technique was used to include the right iron line. In cases where both iron lines causes the absorption line, they were both discarded since they are blended.

In a few cases two iron lines had the same wavelength and EP but different  $\log gf$ . If these both cause an iron line they can be combined into a single line by adding their  $gf$  values. After this step, there was 414 Fe I lines and 12 Fe II lines, respectively.

#### 4.1.1.3 Calibrating $\log gf$

These lines were collected into a single line list in the format required by MOOG (Snedden, 1973) and the line abundance were measured by all lines using the solar atmosphere model described above.

Finish from here...

### 4.1.2 Second version

## 4.2 HD20010

HD 20010 is a star that has been analysed twice with the methodology described here in this thesis. First time this star was analysed was in Andreasen et al. (2016) when the NIR line list was published. Later this line list was revised leading to a removal of several lines. This resulted in the second analysis in Andreasen et al. (2017a); both described below.

### 4.2.1 First analysis

To test our new line list we search for a well-studied solar-type star. The spectrum for such a target needs to be available in the NIR at both high resolution and high S/N. An ideal place to look for such a star is the CRIRES-POP database (Lebzelter et al. 2012). Here, the best target for testing is HD 20010, an F8 subgiant star. This star has been part of many surveys and is therefore well studied. Different parameters from the literature are listed in Table 3. The data available at CRIRES-POP are in the raw format and pipeline reduced, while three small pieces of the spectra are fully reduced on the web page 3 . The data is in the standard CRIRES format with each fits file including four binary tables with the data from the four detectors. In the future, the final reduced data will be presented by the CRIRES-POP team. In contrast to the pipeline reduced data, this will be of higher quality, a better wavelength calibration, and telluric correction. We measured the EWs of the pipeline reduced spectra, and where there was an overlap with the fully reduced spectrum, we measured both as a consistency check. The measured EWs from the fully reduced spectra were consistent with the measured EWs from the pipeline reduced spectra. As mentioned above, we use the Y, J, H, and K-bands which are all available for this star. The spectra come in pieces of 50 Å to 120 Å. These pieces overlap each other, and we were able to measure the EW for a single line up to five times. Unfortunately, wavelength calibration is a difficult task for CRIRES owing to the rather small spectral regions measured on each detector. Each calibration was performed separately for each detector and required the availability of a sufficient number of calibration

lines in the respective spectral region. This was not always the case and a default linear solution was applied. A pipeline reduced spectrum shows up as a stretched spectrum if the wavelength calibration is poor compared to a model spectrum or a solar spectrum, for example. The wavelength calibration does not have any effect on the signal-to-noise ratio, which is generally high for the spectrum of HD 20010. The signal-to-noise varies between 200 and 400 for different chunks. The pipeline reduced spectra for HD 20010 contains tellurics and the wavelength is shifted in radial velocity. All of these factors make the line identification very difficult, and so we developed a program to properly identify the lines, which does the following:

1. Plotting the observed spectrum
2. Overplotting a model spectrum. In this particular case the solar spectrum was used since the atmospheric parameters are close enough, so the sun was able to serve as a model
3. Overplotting a telluric spectrum from the TAPAS web page ([Bertaux et al., 2014](#))
4. Overplotting vertical lines at the location of lines in the list
5. Calculating the cross-correlation function (CCF) for the telluric spectrum with respect to the observed spectrum, locating the maximum value by a Gaussian fit, and using this to shift the telluric spectrum with the found RV;
6. Performing the same as step 5, but for the model
7. Shifting the lines with the same RV as found for the model/solar spectrum.

The final plot shows the shifted spectra, and the CCFs at the sides. An example of the software in use is shown in Fig. 6. The two RVs are part of the title of the plot. Once the lines were identified, the EWs were measured with the `splot` routine in Image Reduction and Analysis Facility (IRAF). The reason not to choose `ARES` for this task was to visually confirm the identification of the line given the relative poor wavelength calibration. We were able to measure 249 Fe I lines and 5 Fe II lines compared to 344 Fe I lines and 13 Fe II lines for the Sun over the whole NIR spectral region. Whenever we had more than one measurement of a line, the average was used for the final EW. We derived the stellar parameters using the standard procedure (see Sect. 2.6) as done for the Sun. Given the relatively low quality of the spectrum of HD 20010 (see below) and because it is not corrected for telluric contamination, we made a cut in EW at 5 m in order to remove the lines which are most affected by contamination from either telluric or other line blends. Additionally, we made a cut in EP at 5.5 eV because the Fe I and Fe II lines usually used for stellar parameter determination in the optical regime are also limited to similar values (see e.g. [Sousa et al., 2008](#)). Higher excitation potential lines are also more likely to be affected by non-LTE effects. When deriving the atmospheric parameters, we made a  $3\sigma$  outlier removal in the abundance iteratively until there were no more outliers present. Since we could only measure 5 Fe II lines, for comparison we also decided to derive parameters using the same method, but we fixed the surface gravity to the reference value. The resulting atmospheric parameters and iron abundances are presented in Table 4. The effective temperature, surface gravity, and metallicity agree within the errors with the literature values. Similar parameters are obtained by fixing  $\log g$  to the average literature value or by leaving it free.

The errors on the atmospheric parameters for HD 20010 are much higher than what is achievable with other measurements in the literature, as presented above in Table 3. In order to explain these errors, we calculated the abundances for all lines which have at least two measurements of the EW. We then calculated the abundances for the highest measured EW and the lowest. The differences in abundances are presented in Fig. 7. The very large differences (more than 0.1 dex) translate to the high errors in the parameters.

The source of the large errors on the parameters can be seen more clearly where abundances are compared to excitation potential or abundances versus reduced EW. Here the dispersion on the abundances can be seen clearly, as shown in Fig. 8.

This test strongly suggest that errors in the EWs, likely due to the poor quality of this spectrum, are responsible for the relatively large error bars in the derived stellar parameters. Systematic errors (e.g. due to a possible non-optimal reduction of the spectrum) may be the reason for these large error bars. As the CRIRES-POP team continue their great efforts in reducing the optimal spectra, it will be interesting to re-visit this star once the entire spectrum has been fully reduced.

### 4.2.2 Second analysis

As a first step we revisit HD 20010 for which we derived atmospheric stellar parameters in Paper I using the newly revised line list presented in this paper. The results are shown in Table 4.1 along with the results for the two other stars analysed in this work. We see better agreement with the average literature values adopted (especially  $[\text{Fe}/\text{H}]$  and  $\log g$ ), and smaller errors with the updated results. This suggests that the new line list is more reliable.

Table 4.1: Results for the three stars with first set of parameters are the literature values as presented in Table. ??, second set of parameters are results with  $\log g$  set to the same value during the minimization procedure as found in the literature (fixed), and last set of parameters are with all parameters free during the minimization procedure.

	HD 20010	10 Leo	Arcturus
Literature			
$T_{\text{eff}}$ (lit.)	$6152 \pm 95$	$4741 \pm 60$	$4300 \pm 110$
$\log g$ (lit.)	$3.96 \pm 0.19$	$2.76 \pm 0.17$	$1.60 \pm 0.29$
$[\text{Fe}/\text{H}]$ (lit.)	$-0.27 \pm 0.06$	$-0.03 \pm 0.02$	$-0.54 \pm 0.11$
$\xi_{\text{micro}}$ (lit.)	$1.17 \pm 0.24$	$1.45 \pm 0.08$	$1.93 \pm 0.13$
$\log g$ fixed			
$T_{\text{eff}}$	$6161 \pm 164$	$4761 \pm 118$	$4357 \pm 74$
$\log g$	$3.96$ (fixed)	$2.76$ (fixed)	$1.60$ (fixed)
$[\text{Fe}/\text{H}]$	$-0.18 \pm 0.11$	$0.01 \pm 0.07$	$-0.55 \pm 0.04$
$\xi_{\text{micro}}$	$1.72 \pm 0.44$	$1.25 \pm 0.11$	$1.55 \pm 0.10$
All free			
$T_{\text{eff}}$	$6162 \pm 184$	$4805 \pm 98$	$4439 \pm 62$
$\log g$	$4.08 \pm 0.77$	$2.42 \pm 0.61$	$1.20 \pm 0.20$
$[\text{Fe}/\text{H}]$	$-0.18 \pm 0.11$	$-0.01 \pm 0.07$	$-0.58 \pm 0.06$
$\xi_{\text{micro}}$	$1.59 \pm 0.49$	$1.23 \pm 0.10$	$1.55 \pm 0.10$

The parameters for the three stars, omitting the Sun since the derived parameters are trivial with a calibrated line list<sup>2</sup>, are presented in Fig. 4.1. We show the literature values (blue), derived parameters

<sup>2</sup> The solar parameters used were:  $T_{\text{eff}} = 5777$  K,  $\log g = 4.44$  dex,  $[\text{Fe}/\text{H}] = 0.00$  dex, and  $\xi_{\text{micro}} = 1.00$  km/s.



with  $\log g$  fixed to the literature value (green), and derived parameters when  $\log g$  is free during the minimization procedure (red points).

### 4.3 Arcturus

Arcturus is one of the brightest stars on the night sky with a V magnitude of -0.05 (Ducati, 2002). Hence it is a prime target for testing with the numerous measurements of the atmospheric parameters as mentioned above.

The atlas consists of both a summer observation set and a winter observation set. The two data sets have been obtained in order to minimise the effect of tellurics at different spectral regions. A comparison between the two sets of measured EWs - both the manual measurements using IRAF and the automatic measurements using ARES - are shown in Fig. ?? . The automatic EW measurements for the summer set and winter set show excellent agreement with a dispersion of 7mÅ. This means that the two data sets are very similar, thus we decided to only manually measure the EWs for one set (summer). We did, however, measure a few lines from the winter data set to verify the agreement. Since the EWs are very similar we chose to only derive parameters of the summer set with EWs measured with ARES . Parameters were derived with and without  $\log g$  set to a fixed value (1.60 dex, the average literature value adopted). The derivation of the parameters followed the procedure presented in Paper I, although we used the minimization routine of FASMA (Andreasen et al., 2017b). After we reached convergence using all the iron lines we were able to measure, one outlier above  $3\sigma$  in abundance were removed, and the minimization routine was restarted. This process was done iteratively until there were no more outliers. The final results are presented in Table 4.1 together with mean parameters from the literature.

We generally see good agreement between the derived parameters and the average values from the literature adopted (see Table 4.1). The only parameter being difficult to measure is the surface gravity due to the low number of Fe II lines in the NIR. It is very important to derive the metallicity accurately, and we report consistent results overall.

### 4.4 10 Leo

The approach for determining the atmospheric stellar parameters for 10 Leo is identical to Arcturus. We use ARES on each band (YJ, H, and K-band) separately. For the small gaps in the spectrum, we simply set the flux to 1, since the spectrum is already normalised. This will also prevent ARES to identify and measure any lines in these regions. The EWs from the three regions are combined to one final line list used for the determination of the parameters. The final results can be seen in Fig. 4.1 and Table 4.1.

Generally the derived parameters are in excellent agreement with the literature values listed here. For  $T_{\text{eff}}$  we were 64K off with  $\log g$  set as a free parameter, well within the errors. The only parameter that show a discrepancy compared to the literature value is  $\xi_{\text{micro}}$  with a difference of 0.22 km/s, which is at the limit of the errors reported. We note that this parameter is not reported in the PASTEL database, and this was a derived parameter from a empirical relation. We were able to derive good  $\log g$  values, although with larger errors compared to the results from the literature.

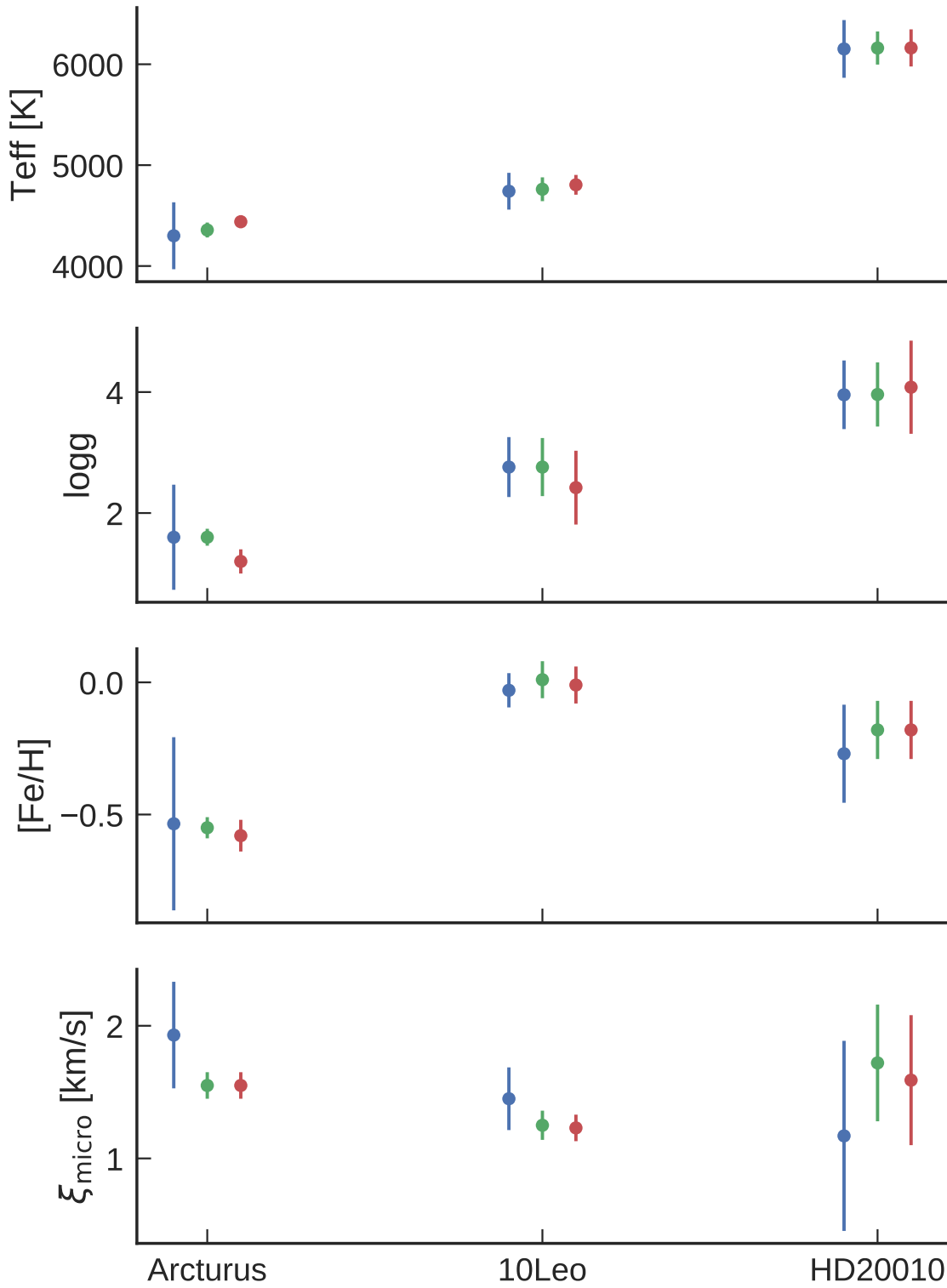


Figure 4.1: Parameters for Arcturus, 10 Leo, and HD 20010 (revisited in this paper). The blue points show the literature values from the PASTEL database as discussed in the text. The green points are the derived values with  $\log g$  fixed to the literature value, and the red points show the derived parameters when  $\log g$  is also derived.

## 4.5 Synthetic cool stars

## 4.6 Parameter dependence on EP cut

It is common practise, as in this case, to make a cut in EP for a line list when deriving parameters. This was suggested in [Andreasen et al. \(2016\)](#) (later done in [Andreasen et al., 2017a](#)) for the NIR line list used here. This cut was made at 5.5 eV, inspired by a similar cut in the optical ([Sousa et al., 2008](#)), including only lines below this limit. The lines with higher EP might also be affected by non-LTE effects which is not treated in this methodology.

As the parameters are dependent on this cut in EP, it seemed interesting to divide a line list in two with upper and lower EPs and analyse those separately. Before going into that analysis it is important to note, that the parameters should not depend on any cut in EP if the theory is right, the radiative transfer code is working properly, and the atmospheric models are correct. Lines with different EP are likely to be formed in different layers of the atmosphere as discussed in [Section 2.2](#), however this should not effect the final derived abundance, which is the problem here.

Make a figure that shows this

## Chapter 5

### Future work

# Bibliography

- Adibekyan, V. Z., Benamati, L., Santos, N. C., Alves, S., Lovis, C., Udry, S., Israelian, G., Sousa, S. G., Tsantaki, M., Mortier, A., Sozzetti, A., and De Medeiros, J. R.: 2015, *MNRAS* **450**, 1900
- Aerts, C., Christensen-Dalsgaard, J., and Kurtz, D. W.: 2010, *Asteroseismology*, Springer-Verlag
- Ammler-von Eiff, M., Santos, N. C., Sousa, S. G., Fernandes, J., Guillot, T., Israelian, G., Mayor, M., and Melo, C.: 2009, *A&A* **507**, 523
- Andreasen, D. T., Sousa, S. G., Delgado Mena, E., Santos, N. C., Lebzelter, T., Mucciarelli, A., and Neil, J. J.: 2017a, *A&A* **585**, A143
- Andreasen, D. T., Sousa, S. G., Delgado Mena, E., Santos, N. C., Tsantaki, M., Rojas-Ayala, B., and Neves, V.: 2016, *A&A* **585**, A143
- Andreasen, D. T., Sousa, S. G., Tsantaki, M., Teixeira, G. D. C., Mortier, A., Santos, N. C., Suárez-Andrés, L., Delgado Mena, E., and Ferreira, A. C. S.: 2017b, *A&A* **600**, A69
- Artigau, É., Kouach, D., Donati, J.-F., Doyon, R., Delfosse, X., Baratchart, S., Lacombe, M., Moutou, C., Rabou, P., Parès, L. P., Micheau, Y., Thibault, S., Reshetov, V. A., Dubois, B., Hernandez, O., Vallée, P., Wang, S.-Y., Dolon, F., Pepe, F. A., Bouchy, F., Striebig, N., Hénault, F., Loop, D., Saddlemyer, L., Barrick, G., Vermeulen, T., Dupieux, M., Hébrard, G., Boisse, I., Martioli, E., Alencar, S. H. P., do Nascimento, J.-D., and Figueira, P.: 2014, in *Society of Photo-Optical Instrumentation Engineers (SPIE) Conference Series*, Vol. 9147 of *Society of Photo-Optical Instrumentation Engineers (SPIE) Conference Series*, p. 15
- Baraffe, I., Homeier, D., Allard, F., and Chabrier, G.: 2015, *A&A* **577**, A42
- Bedding, T. R., Mosser, B., Huber, D., Montalbán, J., Beck, P., Christensen-Dalsgaard, J., Elsworth, Y. P., García, R. A., Miglio, A., Stello, D., White, T. R., De Ridder, J., Hekker, S., Aerts, C., Barban, C., Belkacem, K., Broomhall, A.-M., Brown, T. M., Buzasi, D. L., Carrier, F., Chaplin, W. J., di Mauro, M. P., Dupret, M.-A., Frandsen, S., Gilliland, R. L., Goupil, M.-J., Jenkins, J. M., Kallinger, T., Kawaler, S., Kjeldsen, H., Mathur, S., Noels, A., Silva Aguirre, V., and Ventura, P.: 2011, *Nature* **471**, 608
- Bensby, T., Feltzing, S., and Oey, M. S.: 2014, *A&A* **562**, A71
- Bertaux, J. L., Lallement, R., Ferron, S., Boonne, C., and Bodichon, R.: 2014, *A&A* **564**, A46
- Blackwell, D. E. and Shallis, M. J.: 1977, *MNRAS* **180**, 177

- Bochanski, J. J., Hawley, S. L., Covey, K. R., West, A. A., Reid, I. N., Golimowski, D. A., and Ivezić, Ž.: 2010, *AJ* **139**, 2679
- Boyajian, T. S., von Braun, K., van Belle, G., McAlister, H. A., ten Brummelaar, T. A., Kane, S. R., Muirhead, P. S., Jones, J., White, R., Schaefer, G., Ciardi, D., Henry, T., López-Morales, M., Ridgway, S., Gies, D., Jao, W.-C., Rojas-Ayala, B., Parks, J. R., Sturmann, L., Sturmann, J., Turner, N. H., Farrington, C., Goldfinger, P. J., and Berger, D. H.: 2012, *ApJ* **757**, 112
- Casagrande, L., Portinari, L., and Flynn, C.: 2006, *MNRAS* **373**, 13
- Casagrande, L., Ramírez, I., Meléndez, J., Bessell, M., and Asplund, M.: 2010, *A&A* **512**, A54
- Chaplin, W. J., Kjeldsen, H., Christensen-Dalsgaard, J., Basu, S., Miglio, A., Appourchaux, T., Bedding, T. R., Elsworth, Y., García, R. A., Gilliland, R. L., Girardi, L., Houdek, G., Karoff, C., Kawaler, S. D., Metcalfe, T. S., Molenda-Żakowicz, J., Monteiro, M. J. P. F. G., Thompson, M. J., Verner, G. A., Ballot, J., Bonanno, A., Brandão, I. M., Broomhall, A.-M., Bruntt, H., Campante, T. L., Corsaro, E., Creevey, O. L., Doğan, G., Esch, L., Gai, N., Gaulme, P., Hale, S. J., Handberg, R., Hekker, S., Huber, D., Jiménez, A., Mathur, S., Mazumdar, A., Mosser, B., New, R., Pinsonneault, M. H., Pricopi, D., Quirion, P.-O., Régulo, C., Salabert, D., Serenelli, A. M., Silva Aguirre, V., Sousa, S. G., Stello, D., Stevens, I. R., Suran, M. D., Uytterhoeven, K., White, T. R., Borucki, W. J., Brown, T. M., Jenkins, J. M., Kinemuchi, K., Van Cleve, J., and Klaus, T. C.: 2011, *Science* **332**, 213
- Christensen-Dalsgaard, J., Kjeldsen, H., Brown, T. M., Gilliland, R. L., Arentoft, T., Frandsen, S., Quirion, P.-O., Borucki, W. J., Koch, D., and Jenkins, J. M.: 2010, *ApJL* **713**, L164
- Conod, U., Blind, N., Wildi, F., and Pepe, F.: 2016, in *Society of Photo-Optical Instrumentation Engineers (SPIE) Conference Series*, Vol. 9909 of *Proceedings of the SPIE*, p. 990941
- Czekala, I., Andrews, S. M., Mandel, K. S., Hogg, D. W., and Green, G. M.: 2015, *ApJ* **812**, 128
- Delfosse, X., Donati, J.-F., Kouach, D., Hébrard, G., Doyon, R., Artigau, E., Bouchy, F., Boisse, I., Brun, A. S., Hennebelle, P., Widemann, T., Bouvier, J., Bonfils, X., Morin, J., Moutou, C., Pepe, F., Udry, S., do Nascimento, J.-D., Alencar, S. H. P., Castilho, B. V., Martioli, E., Wang, S. Y., Figueira, P., and Santos, N. C.: 2013, in L. Cambresy, F. Martins, E. Nuss, and A. Palacios (eds.), *SF2A-2013: Proceedings of the Annual meeting of the French Society of Astronomy and Astrophysics*, pp 497–508
- Dotter, A., Chaboyer, B., Jevremović, D., Kostov, V., Baron, E., and Ferguson, J. W.: 2008, *ApJS* **178**, 89
- Ducati, J. R.: 2002, *VizieR Online Data Catalog* 2237
- Follert, R., Dorn, R. J., Oliva, E., Lizon, J. L., Hatzes, A., Piskunov, N., Reiners, A., Seemann, U., Stempels, E., Heiter, U., Marquart, T., Lockhart, M., Anglada-Escude, G., Löwinger, T., Baade, D., Grunhut, J., Bristow, P., Klein, B., Jung, Y., Ives, D. J., Kerber, F., Pozna, E., Paufigue, J., Kaeufl, H. U., Origlia, L., Valenti, E., Gojak, D., Hilker, M., Pasquini, L., Smette, A., and Smoker, J.: 2014, in *Society of Photo-Optical Instrumentation Engineers (SPIE) Conference Series*, Vol. 9147 of *Society of Photo-Optical Instrumentation Engineers (SPIE) Conference Series*, p. 19
- Girardi, L., Bressan, A., Bertelli, G., and Chiosi, C.: 2000, *A&A Supp.* **141**, 371

Gonzalez, G. and Laws, C.: 2000, *AJ* **119**, 390

Gray, D. F.: 2005, *The Observation and Analysis of Stellar Photospheres*, 3rd ed.

Grundahl, F., Fredslund Andersen, M., Christensen-Dalsgaard, J., Antoci, V., Kjeldsen, H., Handberg, R., Houdek, G., Bedding, T. R., Pallé, P. L., Jessen-Hansen, J., Silva Aguirre, V., White, T. R., Frandsen, S., Albrecht, S., Andersen, M. I., Arentoft, T., Brogaard, K., Chaplin, W. J., Harpsøe, K., Jørgensen, U. G., Karovicova, I., Karoff, C., Kjærgaard Rasmussen, P., Lund, M. N., Sloth Lundkvist, M., Skottfelt, J., Norup Sørensen, A., Tronsgaard, R., and Weiss, E.: 2017, *ApJ* **836**, 142

Gustafsson, B., Edvardsson, B., Eriksson, K., Jørgensen, U. G., Nordlund, Å., and Plez, B.: 2008, *A&A* **486**, 951

Hinkle, K. H., Wallace, L., and Livingston, W.: 1995, in A. J. Sauval, R. Blomme, and N. Grevesse (eds.), *Laboratory and Astronomical High Resolution Spectra*, Vol. 81 of *Astronomical Society of the Pacific Conference Series*, p. 66

Huber, D., Silva Aguirre, V., Matthews, J. M., Pinsonneault, M. H., Gaidos, E., García, R. A., Hekker, S., Mathur, S., Mosser, B., Torres, G., Bastien, F. A., Basu, S., Bedding, T. R., Chaplin, W. J., Demory, B.-O., Fleming, S. W., Guo, Z., Mann, A. W., Rowe, J. F., Serenelli, A. M., Smith, M. A., and Stello, D.: 2014, *ApJS* **211**, 2

Husser, T.-O., Wende-von Berg, S., Dreizler, S., Homeier, D., Reiners, A., Barman, T., and Hauschildt, P. H.: 2013, *A&A* **553**, A6

Kippenhahn, R. and Weigert, A.: 1994, *Stellar Structure and Evolution*, Springer-Verlag

Kjeldsen, H. and Bedding, T. R.: 1995, *A&A* **293**, 87

Kotani, T., Tamura, M., Suto, H., Nishikawa, J., Sato, B., Aoki, W., Usuda, T., Kurokawa, T., Kashiwagi, K., Nishiyama, S., Ikeda, Y., Hall, D. B., Hodapp, K. W., Hashimoto, J., Morino, J.-I., Okuyama, Y., Tanaka, Y., Suzuki, S., Inoue, S., Kwon, J., Suenaga, T., Oh, D., Baba, H., Narita, N., Kokubo, E., Hayano, Y., Izumiura, H., Kambe, E., Kudo, T., Kusakabe, N., Ikoma, M., Hori, Y., Omiya, M., Genda, H., Fukui, A., Fujii, Y., Guyon, O., Harakawa, H., Hayashi, M., Hidai, M., Hirano, T., Kuzuhara, M., Machida, M., Matsuo, T., Nagata, T., Onuki, H., Ogihara, M., Takami, H., Takato, N., Takahashi, Y. H., Tachinami, C., Terada, H., Kawahara, H., and Yamamuro, T.: 2014, in *Society of Photo-Optical Instrumentation Engineers (SPIE) Conference Series*, Vol. 9147 of *Society of Photo-Optical Instrumentation Engineers (SPIE) Conference Series*, p. 14

Kupka, F. G., Ryabchikova, T. A., Piskunov, N. E., Stempels, H. C., and Weiss, W. W.: 2000, *Baltic Astronomy* **9**, 590

Kurucz, R.: 1993, *ATLAS9 Stellar Atmosphere Programs and 2 km/s grid. Kurucz CD-ROM No. 13. Cambridge, Mass.: Smithsonian Astrophysical Observatory, 1993*. 13

Lebzelter, T., Heiter, U., Abia, C., Eriksson, K., Ireland, M., Neilson, H., Nowotny, W., Maldonado, J., Merle, T., Peterson, R., Plez, B., Short, C. I., Wahlgren, G. M., Worley, C., Aringer, B., Bladh, S., de Laverny, P., Goswami, A., Mora, A., Norris, R. P., Recio-Blanco, A., Scholz, M., Thévenin, F., Tsuji, T., Kordopatis, G., Montesinos, B., and Wing, R. F.: 2012, *A&A* **547**, A108

Lindgren, S., Heiter, U., and Seifahrt, A.: 2016, *A&A* **586**, A100

Meléndez, J. and Barbuy, B.: 1999, *ApJS* **124**, 527

Mucciarelli, A., Pancino, E., Lovisi, L., Ferraro, F. R., and Lapenna, E.: 2013, *ApJ* **766**, 78

Neuforge-Verheecke, C. and Magain, P.: 1997, *A&A* **328**, 261

Önehag, A., Heiter, U., Gustafsson, B., Piskunov, N., Plez, B., and Reiners, A.: 2012, *A&A* **542**, A33

Origlia, L., Oliva, E., Baffa, C., Falcini, G., Giani, E., Massi, F., Montegriffo, P., Sanna, N., Scuderi, S., Sozzi, M., Tozzi, A., Carleo, I., Gratton, R., Ghinassi, F., and Lodi, M.: 2014, in *Society of Photo-Optical Instrumentation Engineers (SPIE) Conference Series*, Vol. 9147 of *Society of Photo-Optical Instrumentation Engineers (SPIE) Conference Series*, p. 1

Piskunov, N. E., Kupka, F., Ryabchikova, T. A., Weiss, W. W., and Jeffery, C. S.: 1995, *A&A Supp.* **112**, 525

Quirrenbach, A., Amado, P. J., Caballero, J. A., Mundt, R., Reiners, A., Ribas, I., Seifert, W., Abril, M., Aceituno, J., Alonso-Floriano, F. J., Ammler-von Eiff, M., Antona Jiménez, R., Anwand-Heerwart, H., Azzaro, M., Bauer, F., Barrado, D., Becerril, S., Béjar, V. J. S., Benítez, D., Berdiñas, Z. M., Cárdenas, M. C., Casal, E., Claret, A., Colomé, J., Cortés-Contreras, M., Czesla, S., Doellinger, M., Dreizler, S., Feiz, C., Fernández, M., Galadí, D., Gálvez-Ortiz, M. C., García-Piquer, A., García-Vargas, M. L., Garrido, R., Gesa, L., Gómez Galera, V., González Álvarez, E., González Hernández, J. I., Grözing, U., Guàrdia, J., Guenther, E. W., de Guindos, E., Gutiérrez-Soto, J., Hagen, H.-J., Hatzes, A. P., Hauschildt, P. H., Helmling, J., Henning, T., Hermann, D., Hernández Castaño, L., Herrero, E., Hidalgo, D., Holgado, G., Huber, A., Huber, K. F., Jeffers, S., Joergens, V., de Juan, E., Kehr, M., Klein, R., Kürster, M., Lamert, A., Lalitha, S., Laun, W., Lemke, U., Lenzen, R., López del Fresno, M., López Martí, B., López-Santiago, J., Mall, U., Mandel, H., Martín, E. L., Martín-Ruiz, S., Martínez-Rodríguez, H., Marvin, C. J., Mathar, R. J., Mirabet, E., Montes, D., Morales Muñoz, R., Moya, A., Naranjo, V., Ofir, A., Oreiro, R., Pallé, E., Panduro, J., Passegger, V.-M., Pérez-Calpena, A., Pérez Medialdea, D., Perger, M., Pluto, M., Ramón, A., Rebolo, R., Redondo, P., Reffert, S., Reinhardt, S., Rhode, P., Rix, H.-W., Rodler, F., Rodríguez, E., Rodríguez-López, C., Rodríguez-Pérez, E., Rohloff, R.-R., Rosich, A., Sánchez-Blanco, E., Sánchez Carrasco, M. A., Sanz-Forcada, J., Sarmiento, L. F., Schäfer, S., Schiller, J., Schmidt, C., Schmitt, J. H. M. M., Solano, E., Stahl, O., Storz, C., Stürmer, J., Suárez, J. C., Ulbrich, R. G., Veredas, G., Wagner, K., Winkler, J., Zapatero Osorio, M. R., Zechmeister, M., Abellán de Paco, F. J., Anglada-Escudé, G., del Burgo, C., Klutsch, A., Lizon, J. L., López-Morales, M., Morales, J. C., Perryman, M. A. C., Tulloch, S. M., and Xu, W.: 2014, in *Society of Photo-Optical Instrumentation Engineers (SPIE) Conference Series*, Vol. 9147 of *Society of Photo-Optical Instrumentation Engineers (SPIE) Conference Series*, p. 1

Ramírez, I. and Meléndez, J.: 2005a, *ApJ* **626**, 446

Ramírez, I. and Meléndez, J.: 2005b, *ApJ* **626**, 465

Rayner, J., Bond, T., Bonnet, M., Jaffe, D., Muller, G., and Tokunaga, A.: 2012, in *Ground-based and Airborne Instrumentation for Astronomy IV*, Vol. 8446 of *Proceedings of the SPIE*, p. 84462C



- Rayner, J., Tokunaga, A., Jaffe, D., Bonnet, M., Ching, G., Connelley, M., Kokubun, D., Lockhart, C., and Warmbier, E.: 2016, in *Society of Photo-Optical Instrumentation Engineers (SPIE) Conference Series*, Vol. 9908 of *Proceedings of the SPIE*, p. 990884
- Recio-Blanco, A., Bijaoui, A., and de Laverny, P.: 2006, *MNRAS* **370**, 141
- Santos, N. C., Sousa, S. G., Mortier, A., Neves, V., Adibekyan, V., Tsantaki, M., Delgado Mena, E., Bonfils, X., Israelian, G., Mayor, M., and Udry, S.: 2013, *A&A* **556**, A150
- Snedden, C. A.: 1973, *Ph.D. thesis*, THE UNIVERSITY OF TEXAS AT AUSTIN.
- Sousa, S. G., Santos, N. C., Adibekyan, V., Delgado-Mena, E., and Israelian, G.: 2015, *A&A* **577**, A67
- Sousa, S. G., Santos, N. C., Israelian, G., Mayor, M., and Monteiro, M. J. P. F. G.: 2007, *A&A* **469**, 783
- Sousa, S. G., Santos, N. C., Mayor, M., Udry, S., Casagrande, L., Israelian, G., Pepe, F., Queloz, D., and Monteiro, M. J. P. F. G.: 2008, *A&A* **487**, 373
- Torres, G., Andersen, J., and Giménez, A.: 2010, *Astronomy and Astrophysics Reviews* **18**, 67
- Torres, G., Fischer, D. A., Sozzetti, A., Buchhave, L. A., Winn, J. N., Holman, M. J., and Carter, J. A.: 2012, *ApJ* **757**, 161
- Torres, G., Winn, J. N., and Holman, M. J.: 2008, *ApJ* **677**, 1324
- Tsantaki, M., Andreasen, D. T., Teixeira, G. D. C., Sousa, S. G., Santos, N. C., Delgado-Mena, E., and Bruzual, G.: 2017, *MNRAS* **555**, A150
- Tsantaki, M., Sousa, S. G., Adibekyan, V. Z., Santos, N. C., Mortier, A., and Israelian, G.: 2013, *A&A* **555**, A150
- Tsantaki, M., Sousa, S. G., Santos, N. C., Montalto, M., Delgado-Mena, E., Mortier, A., Adibekyan, V., and Israelian, G.: 2014, *A&A* **570**, A80
- Valenti, J. A. and Fischer, D. A.: 2005, *ApJS* **159**, 141
- Valenti, J. A. and Piskunov, N.: 1996, *A&A Supp.* **118**, 595